JOURNAL OF PETROLOGY | VOLUME 47 | NUMBER 1 | PAGES 97–118 | 2006 | doi:10.1093/petrology/egi069

Monazite–Xenotime Thermochronometry and Al_2SiO_5 Reaction Textures in the Picuris Range, Northern New Mexico, USA: New Evidence for a 1450–1400 Ma Orogenic Event

CHRISTOPHER G. DANIEL[1]* AND JOSEPH M. PYLE[2]

[1]DEPARTMENT OF GEOLOGY, BUCKNELL UNIVERSITY, LEWISBURG, PA 17837, USA

[2]DEPARTMENT OF EARTH AND ENVIRONMENTAL SCIENCES, RENSSELAER POLYTECHNIC INSTITUTE, TROY, NY 12180–3590, USA

RECEIVED NOVEMBER 2, 2004; ACCEPTED JUNE 30, 2005
ADVANCE ACCESS PUBLICATION AUGUST 18, 2005

Al_2SiO_5 reaction textures in aluminous schist and quartzite of the northern Picuris range, north-central New Mexico, record a paragenetic sequence of kyanite to sillimanite to andalusite, consistent with a clockwise P–T *loop, with minor decompression near the Al_2SiO_5 triple-point. Peak metamorphic temperatures are estimated at 510–525°C, at 4·0–4·2 kbar. Kyanite and fibrolite are strongly deformed; some prismatic sillimanite, and all andalusite are relatively undeformed. Monazite occurs as inclusions within kyanite, mats of sillimanite and centimetre-scale porphyroblasts of andalusite, and is typically aligned subparallel to the dominant regional foliation (S_0/S_1 or S_2) and extension lineation (L_1). Back-scatter electron images and X-ray maps of monazite reveal distinct core, intermediate and rim compositional domains. Monazite–xenotime thermometry from the intermediate and rim domains yields temperatures of 405–470°C (±50°C) and 500–520°C (±50°C), respectively, consistent with the prograde to peak metamorphic growth of monazite.* In situ, *ion microprobe analyses from five monazites yield an upper intercept age of 1417 ± 9 Ma. Near-concordant to concordant analyses yield ^{207}Pb–^{206}Pb ages from 1434 ± 12 Ma (core) to 1390 ± 20 Ma (rim). We find no evidence of older regional metamorphism related to the ~1650 Ma Mazatzal Orogeny.*

KEY WORDS: *Al_2SiO_5; metamorphism; monazite; thermochronometry; triple-point*

INTRODUCTION

Several recent studies (Karlstrom *et al.*, 1997, 2004; Pedrick *et al.*, 1998; Read *et al.*, 1999; Williams *et al.*, 1999) hypothesize that Proterozoic rocks in north-central New Mexico (Fig. 1) experienced distinct tectonothermal events at ~1650 and ~1400 Ma. They propose that regional amphibolite to near-granulite facies metamorphism and north-vergent folding and thrusting was related to the Mazatzal Orogeny (~1650 Ma). Subsequent overprinting by amphibolite facies metamorphism at ~1400 Ma was accompanied by the reactivation of pre-existing (~1650 Ma) regional deformational fabrics. The ~1400 Ma thermal event is interpreted to reflect a major basaltic underplating event at the base of the crust (Williams *et al.*, 1999; Karlstrom *et al.*, 2004). This proposed thermal perturbation provides a mechanism to reset the argon systematics within older ~1650 Ma metamorphic minerals, such as hornblende and muscovite, and cause new metamorphic minerals to grow or overgrowths to form on pre-existing minerals.

With respect to the Al_2SiO_5 'triple-point' rocks of northern New Mexico (Holdaway, 1978; Grambling, 1981; Grambling & Williams, 1985), Karlstrom *et al.* (1997) proposed "...polymetamorphism of the middle crust with *P–T* paths close to the alumino-silicate triple-point at both 1·65 and 1·4 Ga. A consequence of this

*Corresponding author. Telephone: (570) 577-1133. Fax: (570) 577-3031. E-mail: cdaniel@bucknell.edu

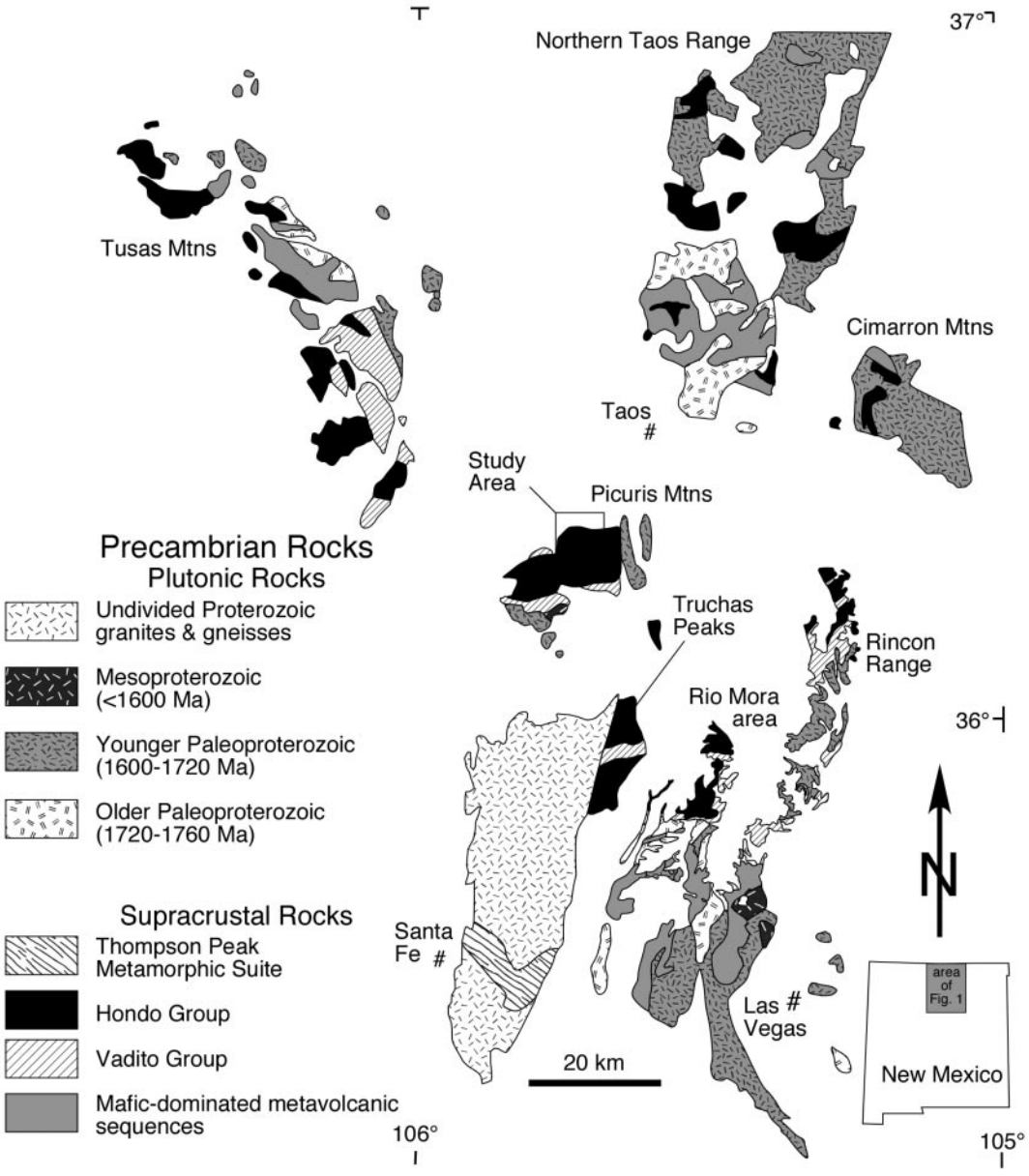

Fig. 1. Generalized geologic map of Proterozoic rocks in north-central New Mexico. Study area is located near centre of map area (modified from Williams *et al.*, 1999).

complex thermal history is growth (and overgrowth) of amphibolite-grade minerals at both 1·65 and 1·4 Ga." The studies by Karlstrom *et al.* (1997), Pedrick *et al.* (1998) and Read *et al.* (1999) briefly discuss the possibility of a single regional tectonothermal event around 1400 Ma, but dismiss it in favor of the polymetamorphic hypothesis. Recent electron microprobe dating of monazite in the Tusas range (Fig. 1; Kopera *et al.*, 2002*a*, 2002*b*) reveals a spread of ages from >1700 to ~1400 Ma that are interpreted to reflect some component of 1450–1400 Ma deformation and metamorphism superimposed upon earlier Mazatzal (~1650 Ma) deformation and metamorphism. Monazite core ages ≥1700 Ma are interpreted as detrital.

The primary goal of this work is to investigate the timing and nature of the Al_2SiO_5 'triple-point' metamorphism in rocks of the northern Picuris Range (Fig. 1). To the best of our knowledge, this study is the first in northern New Mexico to utilize *in situ* analysis of monazite to constrain both the temperature and timing of monazite growth, yielding a relatively well-defined point in the *T*–*t* history of our samples. We also document the timing of

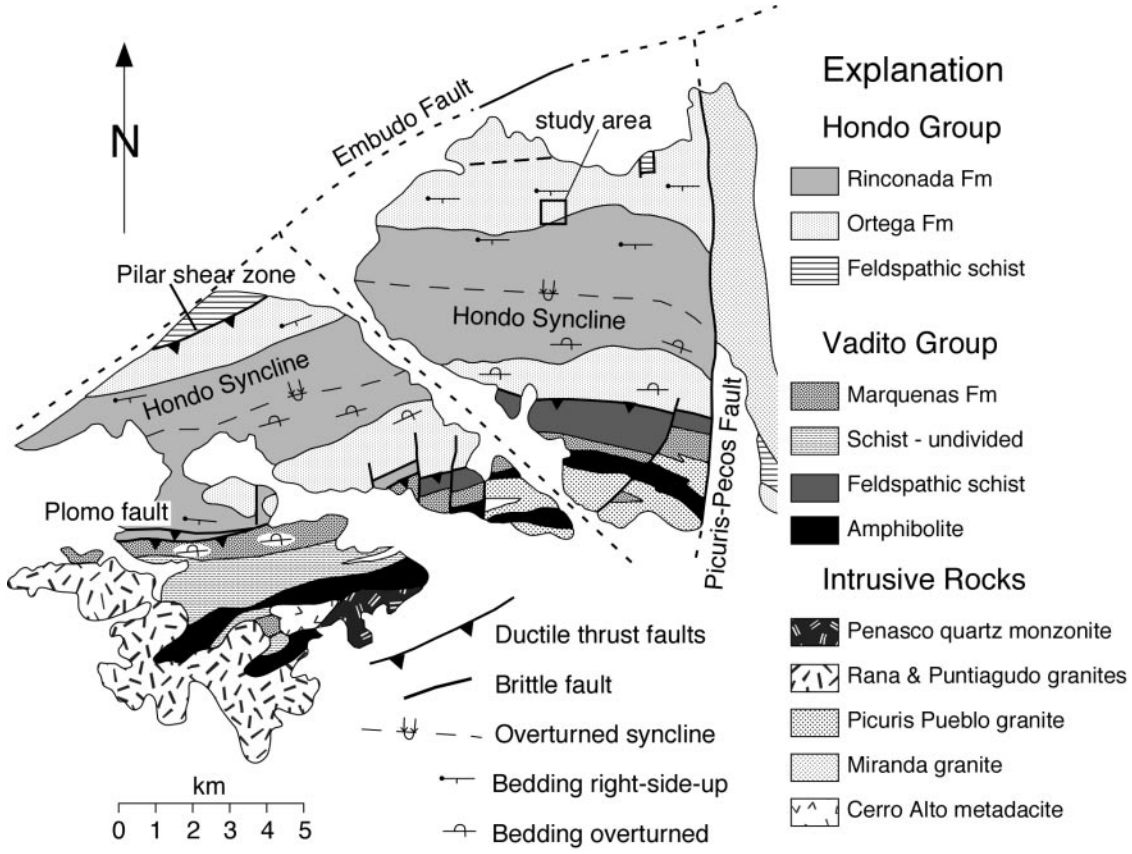

Fig. 2. Simplified geologic map of the Picuris range showing the approximate location for samples used in this study (modified from Bauer, 1993).

monazite growth relative to the Al_2SiO_5 polymorphs and the regional deformational fabrics to constrain the absolute timing of the regional metamorphism and deformation. Such data are key in evaluating and refining models for the Proterozoic tectonic evolution of the southwestern USA.

GEOLOGIC SETTING OF THE PICURIS RANGE

Numerous works document and discuss the geology (Fig. 2), metamorphism and deformational history of the Picuris range (Montgomery, 1953; Long, 1974; Holdaway, 1978; Bell, 1985; Grambling & Williams, 1985; Bauer, 1988, 1993; Holdaway & Goodge, 1990; Bauer & Kelson, 1997; Williams *et al.*, 1999). The 'triple-point' rocks examined in this study were collected from quartzite and aluminous schist within the Ortega Formation (Bauer & Williams, 1989), on the northern limb of the Hondo syncline (Fig. 2). This area is approximately 1 km north of the area studied by Holdaway & Goodge (1990). Metamorphic *P–T* conditions in this area were previously estimated at ~530°C, 4 kbar based upon Grt–Bt thermometry and Al_2SiO_5 phase equilibria (Grambling & Williams, 1985; Holdaway & Goodge, 1990).

The Hondo syncline (Fig. 2) and other major map-scale and outcrop-scale folds were interpreted as second-generation folds (F_2) by Bauer (1993). Ductile high-strain zones (Fig. 2) bound the Ortega and Rinconada formations to the north (Pilar shear zone) and south (Plomo fault). Bedding (S_0) is well preserved within the cross-bedded quartzite of the Ortega and the overlying Rinconada formations. A near-bedding parallel schistosity (S_1) and associated down-dip extension lineation (L_1) are observed within the quartzites. S_1 may be related to rootless, small-scale, intrafolial, isoclinal folds, preserved within the schists of the Rinconada Formation. Both S_0, S_1 and L_1 are folded by F_2-folds. Within schistose units, S_1 is transposed into an east-striking, moderate to steeply south-dipping foliation (S_2). S_2 transects the F_2 folds and is interpreted to have formed relatively late in the development of the F_2 folds (Bauer, 1993). In the quartzites of the northern Picuris, Bauer noted that S_1 and L_1 in the northernmost quartzite continued development during F_2 folding and probably represent a transposed composite foliation and lineation. Bauer (1993) proposed that the

shearing and multiple generations of folds and foliations formed during a single progressive deformation.

DATA AND INTERPRETATIONS

Petrography of the Al_2SiO_5 and associated minerals

Ten oriented samples of Ortega Formation quartzite and five oriented samples of schist were collected during fieldwork in the summers of 1994 and 2000. Quartzites were cut perpendicular to S_1/S_0 and parallel to L_1. Schists were cut perpendicular to the intersection lineation ($L_{1/2}$) of S_1 and S_2; in addition, a second cut was made perpendicular to S_1 and parallel to $L_{1/2}$. Quartzite samples (Fig. 3a and b) are characterized by the mineral assemblage quartz, kyanite, sillimanite, chloritoid, muscovite, hematite–ilmenite, tourmaline ± andalusite. Schist samples (Fig. 3c–f) were collected across a single layer approximately 4–5 m thick. These samples are characterized by large (4–10 cm diameter) andalusite porphyroblasts, abundant muscovite, both prismatic and fibrolitic sillimanite, kyanite, chloritoid, chlorite ± staurolite, hematite–ilmenite, and tourmaline. Accessory minerals, including monazite, xenotime, zircon and apatite, were observed in all samples.

Relative timing of the Al_2SiO_5 polymorphs

Kyanite is strongly deformed, fractured and embayed, and shows polymorphic replacement by sillimanite or andalusite (Fig. 3a, b and d). Many kyanite grains also show partial replacement by muscovite. Kyanite is aligned parallel to S_0/S_1 and L_1 in the quartzite. Ilmenite–hematite inclusions within kyanite are common, and are also aligned parallel to S_0/S_1 and L_1. Similar textures are observed within the schist samples, though kyanite and ilmenite–hematite are observed in both S_1 and S_2. These observations are consistent with earlier work by Holdaway (1978), Bauer (1988, 1993) and Holdaway & Goodge (1990), and suggest kyanite growth during progressive regional S_1 and L_1 deformation.

Sillimanite generally occurs as fibrolite or as fine, prismatic crystals in quartzites (Fig. 3a and b), and both fibrolite and large prismatic crystals up to 20 mm long in the schist samples (Fig. 3c–f). In the northern quartzite, sillimanite is generally aligned in S_1 and L_1. Elsewhere, sillimanite needles are generally undeformed (Holdaway, 1978; Holdaway & Goodge 1990; Bauer, 1993). Fibrolite in the schist occurs within large andalusite porphyroblasts (Fig. 3c and f), and within muscovite in the surrounding matrix. Bent and folded fibrolite are observed within andalusite porphyroblasts (Fig. 3f). Prismatic sillimanite crystals are oriented both parallel to and at a high angle to S_2 (Fig. 3d and e), and contain inclusions of titanhematite aligned parallel to S_2. We interpret these relations to indicate that prismatic sillimanite growth was syn- to post S_2. Prismatic sillimanite cross-cuts kyanite; it is only observed as inclusions within andalusite, and typically shows fractures and embayments, patchy extinction and partial replacement by muscovite or andalusite. The crenulated fibrolite (Fig. 3f) pre-dates the prismatic sillimanite (Fig. 3e).

A large (8–10 cm diameter) andalusite porphyroblast with inclusions of kyanite and sillimanite aligned parallel to L_1 was observed in a thin (1–2 cm) compositional layer within one quartzite sample. Within the schist layer, andalusite poikiloblasts (5–10 cm diameter) form up to ~70% of the rock. They contain abundant inclusions of kyanite, sillimanite, quartz, muscovite, chloritoid and ilmenite–hematite (Fig. 3c–f). Andalusite replaces both kyanite and sillimanite, consistent with direct polymorphic replacement; in addition, andalusite also pseudomorphs muscovite and both kyanite and sillimanite are commonly rimmed by muscovite, consistent with the multi-step reaction mechanism proposed by Carmichael (1969). Poikiloblasts are optically continuous and overgrow a spaced crenulation cleavage defined by muscovite. These textures suggest that andalusite overgrows an intermediate to late stage of S_2 (Fig. 3e and f). There is a weak deflection of the matrix foliation around these andalusite porphyroblasts that reflects minor, post-andalusite deformation.

Locally, kyanite, sillimanite and andalusite show minor, patchy alteration to pyrophyllite, consistent with observations by Bauer (1993). The occurrence of strongly deformed, embayed kyanite, crenulated fibrolite and embayed prismatic sillimanite within relatively undeformed andalusite shows that andalusite growth postdates both fibrolite and prismatic sillimanite for these aluminous bulk compositions.

Relative timing of chloritoid and staurolite

Chloritoid (Fig. 3b) is present in many samples of schist and quartzite but the modal abundance is always small, visually estimated at ≤1–2%. Chloritoid is commonly in contact with kyanite, sillimanite or andalusite; less common are chloritoid pseudomorphs after muscovite, and grains with partial retrograde alteration to chlorite. Chloritoid is generally deformed and aligned in S_1/S_2. Staurolite is observed in the schist samples but not the quartzite samples, consistent with observations by Holdaway (1978) and Holdaway & Goodge (1990). Staurolite occurs as millimetre-scale, subhedral to euhedral crystals, with a pale bluish-grey colour in plane-polarized light and very weak pleochroism; modal abundance estimated visually is ≤1–2%. Staurolite shows little evidence of strain or dissolution and is interpreted to be late or post S_2.

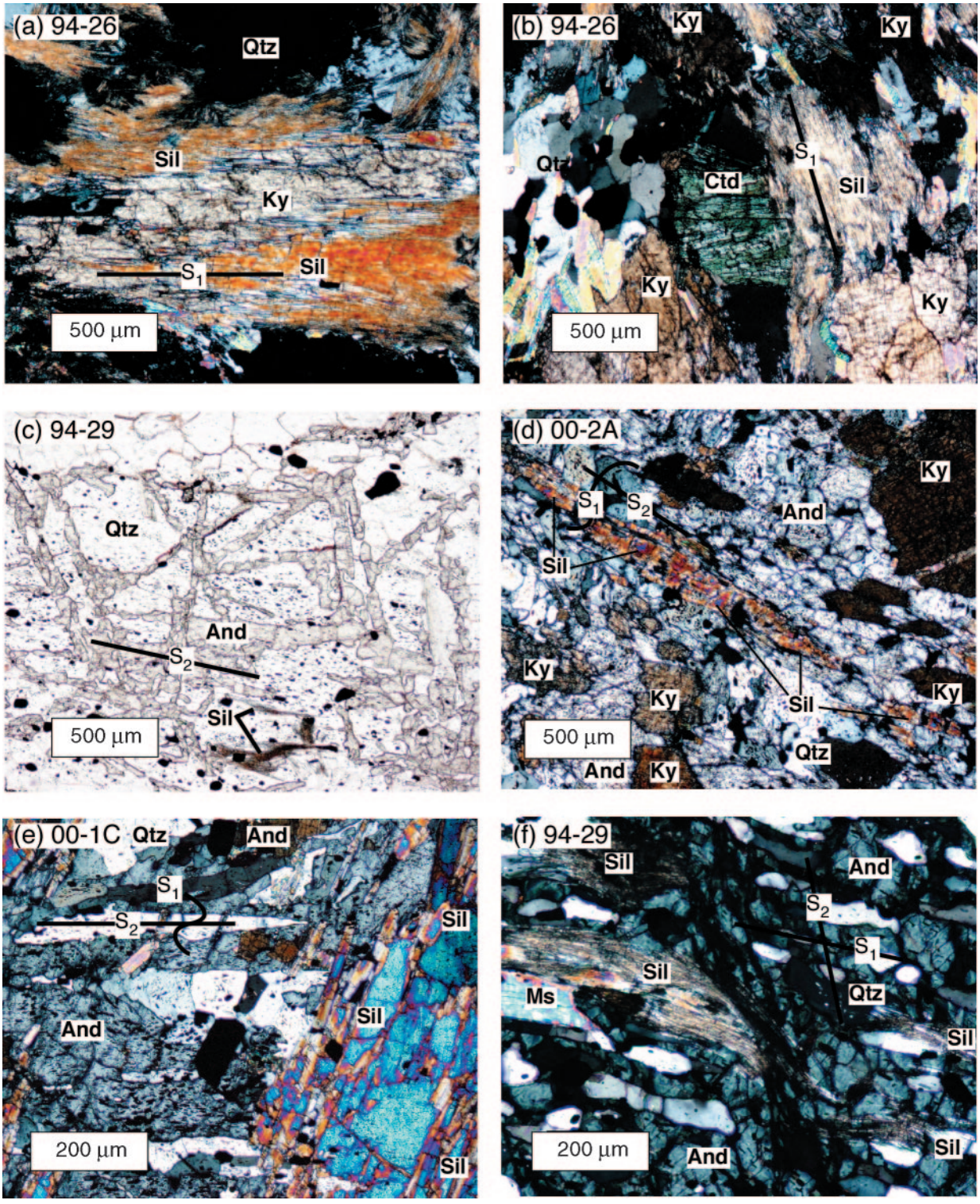

Fig. 3. Digital photomicrographs of Al_2SiO_5 reaction textures in cross-polarized and plane-polarized light. (a) Quartzite sample showing partial replacement of kyanite by sillimanite, both aligned parallel to S_1 and L_1. (b) Quartzite sample with coexisting kyanite, sillimanite and chloritoid. (c) Schist sample with optically continuous andalusite pseudomorphs after muscovite. (d) Schist sample with kyanite and prismatic sillimanite, aligned parallel to S_2, overgrown by post-S_2 poikiloblastic andalusite. (e) Andalusite and prismatic sillimanite overgrowing titanhematite aligned in S_2. (f) Schist sample with crenulated sillimanite needles included within a large, relatively undeformed andalusite poikiloblast.

Table 1: Al_2SiO_5 microprobe analyses

Sample:	94–26		00–2A		
	Ky	Sil	Ky	Sil	And
wt % oxide					
SiO_2	36·93	37·93	38·22	38·00	37·82
Al_2O_3	61·61	60·99	61·67	61·62	60·78
TiO_2	n.d.	n.d.	n.d.	n.d.	n.d.
Fe_2O_3	0·61	0·58	0·76	0·87	1·67
Mn_2O_3	n.d.	n.d.	n.d	n.d.	n.d.
Total	99·20	99·51	100·70	100·51	100·36
Cations on the basis of 5 oxygen					
Si	1·010	1·030	1·031	1·025	1·020
Al	1·980	1·950	1·961	1·959	1·933
Ti	0·000	0·000	0·000	0·000	0·000
Fe^{3+}	0·013	0·012	0·016	0·019	0·036
Mn^{3+}	0·000	0·000	0·000	0·000	0·000
Fe/(Fe+Al)	0·007	0·006	0·008	0·009	0·018

n.d., below detection limit.

Table 2: Chloritoid and staurolite microprobe analyses

Sample:	94–26 Cld	00–2A Cld	00–2A St[1]
wt % oxide			
SiO_2	25·05	25·40	28·05
Al_2O_3	38·02	39·21	54·59
TiO_2	0·02	0·09	0·33
FeO	27·45	22·22	7·12
MnO	0·26	3·85	1·05
MgO	0·68	1·71	0·56
ZnO	n.a.	n.a.	5·01
Total	91·52	92·49	96·75
Cations on the basis of 8 cations			Si + Al = 25·531
Si	2·130	2·115	7·750
Al	3·811	3·848	17·781
Ti	0·001	0·006	0·068
Fe	1·952	1·547	1·645
Mn	0·019	0·272	0·247
Mg	0·087	0·212	0·231
Zn			1·022
H+Li[2]			5·10
Mg/(Fe+Mg)	0·043	0·121	0·123

[1]Staurolite recalculation after Holdaway *et al.* (1988).
[2]Estimated by subtracting total charge from 96 (after Holdaway *et al.*, 1988).
n.a., not analysed.

Chemistry of the Al_2SiO_5 and associated minerals

Methods

Given the nearly identical mineral assemblages within the quartzite samples and the schist samples, we selected one quartzite (94–26) and one schist (00–2a) for major element analyses of kyanite, sillimanite, andalusite, muscovite, staurolite, chloritoid and ilmenite–hematite. Average Al_2SiO_5 analyses are given in Table 1 and representative chloritoid and staurolite analyses are given in Table 2. Major element analyses of the rock-forming minerals and all monazite and xenotime chemical analyses were performed on the JEOL 733 Superprobe electron microprobe housed in the Department of Earth and Environmental Sciences at Rensselaer Polytechnic Institute (RPI). Major element silicate and oxide mineral analyses were conducted at 15 kV, 20 nA with a spot size of 1–5 μm using natural standards for calibration.

Results

Kyanite and sillimanite within the quartzites contain 0·61 and 0·58 wt % Fe_2O_3, respectively. Within the schist samples, kyanite and sillimanite contain 0·76 and 0·87 wt % Fe_2O_3; andalusite contains 1·67 wt % Fe_2O_3. Mn_2O_3 was below detection limits in all Al_2SiO_5 polymorphs. Ilmenite–hematite compositions in the quartzite are variable, with analyses that range from $Hem_{95}Ilm_5$ to $Hem_{53}Ilm_{47}$, suggesting the presence of exsolved ilmenite and hematite domains. Ilmenite–hematite compositions from the schists are uniformly titanhematite ($Hem_{91–94}Ilm_{9–6}$). Ilmenite–hematite from both samples showed no measurable Mg or Mn. Chloritoid Mg/(Fe+Mg) varies from 0·043 in the quartzites to 0·121 in the schists. Chloritoid from the schist contains significantly higher MnO concentrations (MnO = 3·85 wt %) relative to chloritoid from the quartzites (MnO = 0·26 wt %). Staurolite contains 5–6 wt % Zn, ∼1 wt % MnO, with Mg/(Fe+Mg) = 0·12. Mineral compositions are generally consistent with analyses previously reported by Holdaway & Goodge (1990) for similar bulk compositions. The Al_2SiO_5 polymorphs analysed in this study contain significantly more Fe^{3+} than analyses reported by Grambling & Williams (1985) for the Picuris range.

P–T estimates of the 'triple-point' rocks

The occurrence of sillimanite + chloritoid but no staurolite in the quartzite samples places an upper limit on the temperature of metamorphism (Fig. 4; reaction (1)):

$$\text{Fe-chloritoid} + Al_2SiO_5 = \text{Fe-staurolite} + Qtz + H_2O. \quad (1)$$

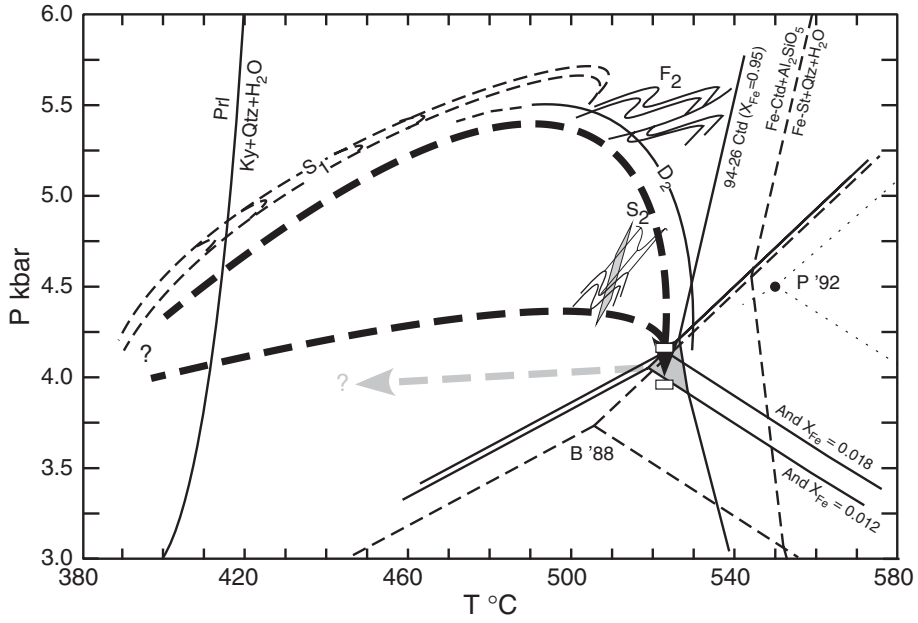

Fig. 4. Peak metamorphic *P–T* conditions (grey triangle) and speculative *P–T–D* paths based upon kyanite, sillimanite, andalusite, chloritoid and staurolite reaction textures and compositions discussed in text. Small white boxes represent *P–T* conditions determined by Holdaway & Goodge (1990). Al_2SiO_5 triple-points from Pattison (P; 1992) and Berman (B; 1988) shown in dotted and dashed lines, respectively. Timing of deformational events S_1 schistosity, F_2 folding and S_2 transecting cleavage (Bauer, 1993) are approximate and vary somewhat across the Picuris range.

Experimental determinations for reaction (1) (Richardson, 1968; Rao & Johannes, 1979) place it at temperatures below the Pattison (1992) Al_2SiO_5 triple-point (Fig. 4), inconsistent with the interpreted equilibrium assemblage of sillimanite + chloritoid. Thus, we retain the Berman (1988) Al_2SiO_5 phase diagram (Fig. 4) utilized by Holdaway & Goodge (1990) and follow their methods and assumptions to calculate the temperature offset (at 4 kbar) for the reaction that results from the substitution of Mg and Mn into chloritoid in equilibrium with a hypothetical staurolite.

In the Fe-rich quartzites, chloritoid compositions of $X_{Fe} = 0{\cdot}96$ correspond to a temperature shift of approximately $-20°C$ (continuous line, Fig. 4), consistent with previous estimates by Holdaway & Goodge (1990), who estimated an error of ~50% on ΔT. This method of determining reaction offset is best applied to minerals with only small deviations from end-member compositions, and is not appropriate for the Zn-rich staurolite. Clearly, the incorporation of Zn+Mn, and possibly Li, stabilized staurolite to a temperature below ~525°C.

Offsets for the Al_2SiO_5 phase equilibria were determined in a similar manner using the substitution of Fe^{3+} for Al^{3+}. Based upon the average partition coefficients from Holdaway & Goodge (1990), a hypothetical andalusite in equilibrium with kyanite and sillimanite from the quartzite samples would have $X_{Fe_2SiO_5} = 0{\cdot}012$. This amount of Fe substitution in andalusite shifts the andalusite–sillimanite reaction up approximately 500 bar. The lack of andalusite in the quartzite sample requires metamorphic pressures greater than approximately 4·0 kbar (Fig. 4). In the schist sample, measured andalusite compositions of $X_{Fe_2SiO_5} = 0{\cdot}018$ produce an offset of approximately 700 bar and require pressures below ~4·2 kbar for the growth of andalusite. Holdaway & Goodge (1990) estimated errors of ~50% on ΔP. Our results (Fig. 4) are nearly identical to those of Holdaway & Goodge (1990), and constrain peak metamorphic temperatures to between ~510°C (lower limit for sillimanite stability) and $525 \pm 10°C$, at pressures near 4·1 kbar ± 100 bar.

Proposed *P–T–D* path

The aluminium silicate textural relationships show early kyanite growth followed by sillimanite and, finally, andalusite growth, consistent with a clockwise loop around the Al_2SiO_5 triple-point with a component of decompression (Fig. 4). The early nature of the *P–T* loop is not well constrained, but probably falls somewhere between the two dashed lines. The *P–T* path of near-isobaric heating is similar to one proposed by Holdaway (1978), though his *P–T* path was placed below the triple-point based upon an inferred Al_2SiO_5 reaction sequence of kyanite to andalusite to sillimanite. The looping *P–T* path of heating and compression followed by approximately 1–1·5 kbar of near-isothermal decompression is based

upon Gibbs method modelling of garnet zoning from the Picuris, and both Fe^{3+} and Mn^{3+} compositional zoning patterns in andalusite from the Rio Mora area (Daniel, 1992). We favor the *P–T* path of heating and compression, given the compressional style of deformation; however, the amount of decompression is poorly constrained.

Kyanite, sillimanite and chloritoid are commonly aligned in S_1/S_2 and L_1. S_2 develops late in the history of folding and is the dominant regional foliation. Andalusite and some prismatic sillimanite overgrow S_2, showing that peak metamorphic temperatures outlasted much of the regional shortening (D_2) indicated by F_2 and S_2. Based upon ^{40}Ar–^{39}Ar ages in the region (Karlstrom *et al.*, 1997), these rocks experienced very slow cooling and probably remained at midcrustal depths of ~12–15 km for 100–200 Myr. This extended residence time at elevated temperatures is responsible for the establishment of the sub-horizontal Al_2SiO_5 isograds documented by Grambling (1981) and Grambling & Williams (1985) in the adjacent Truchas Peaks and Rio Mora areas.

It is important to note that Holdaway & Goodge (1990) interpreted the offset of the andalusite–sillimanite reaction to be the result of a difference in fluid pressure (P_f) between quartzite and schist. Based upon the observed Al_2SiO_5 reaction textures from our study, we interpret the difference in pressure to be the result of different bulk-rock compositions equilibrating at slightly different pressures along a near-isothermal decompressional *P–T* path.

Monazite and xenotime petrography

Three samples of quartzite (94–23, 94–26 and 94–27) and two schist samples (00–2a and 00–3c) were selected for detailed analysis of monazite and xenotime. Monazite occurs as subhedral crystals ranging in size from 5 × 10 to 30 × 100 μm. They are observed as inclusions within kyanite (Fig. 5a), mats of fibrolite (Fig. 5b), andalusite (Fig. 5d and e), titanhematite and matrix muscovite (Fig. 5f). Matrix monazite commonly occur along quartz grain boundaries, Al_2SiO_5–quartz grain boundaries (Fig. 5c) and titanhematite–quartz grain boundaries. In the quartzites, titanhematite inclusions within monazite are aligned parallel to S_1 and L_1, and the monazite grains themselves are also aligned parallel to S_1 and L_1 (Fig. 5a–c). Monazite grains in schist samples are commonly included within andalusite, oriented parallel to S_2 (Fig. 5d) and contain titanhematite inclusions aligned in S_2 (Fig. 5e). A few grains are oriented perpendicular to S_2. Matrix monazite are commonly aligned in S_2 and included within foliated muscovite (Fig. 5f).

Monazite and xenotime chemistry

Methods

Monazite and xenotime grains were located by back-scattered electron (BSE) mapping of polished thin sections and energy dispersive spectroscopy (EDS) analysis. BSE mapping was performed both at RPI and with an FEI Quanta 400 ESEM equipped with an EDAX Genesis 4000 EDS system, located in the Department of Geology at Bucknell University. Monazite and xenotime grains were then examined with a petrographic microscope and photographed to document textural relationships with the rock-forming minerals and deformational fabrics. Selected monazite grains were mapped to characterize the distribution of Y, U, Th and Pb, or Ce, Ca, Y, Th and U using the program *X-ray Map*, coded by F. Spear and D. Wark. Mapping conditions included an accelerating voltage of 25 keV, Faraday cup current of 200–250 nA, pixel size of 0·2–2·0 mm and dwell times of 50–100 ms/pixel. Element maps were processed with the freeware program *NIH Image*.

Analytical conditions for quantitative monazite and xenotime analyses include 15 kV accelerating voltage, 50 nA Faraday cup current and count times of 20–100 s. For monazite, analysed elements (with approximate detection limit in wt %) include Si (0·02), P (0·47), Ca (0·01), Y (0·04), La (0·14), Ce (0·14), Pr (0·13), Nd (0·17), Sm (0·10), Gd (0·11), Tb (0·10), Dy (0·05), Er (0·05), Th (0·09), U (0·06) and Pb (0·11). Elements analysed in xenotime include Si (0·02), P (0·67), Ca (0·01), Y (0·11), Nd (0·07), Sm (0·06), Eu (0·06), Gd (0·07), Tb (0·08), Dy (0·08), Ho (0·10), Er (0·08), Tm (0·06), Yb (0·07), Th (0·12), U (0·07) and Pb (0·11). Standards include synthetic REE and Y phosphates, apatite, Th and Pb silicate, and U oxide.

The complexity of wavelength dispersive spectroscopy (WDS) analysis of minerals with high numbers of L-line and M-line generating elements, and potential interferences, is well known (Roeder, 1985). X-ray lines common to both the monazite and xenotime analytical protocols are Si Kα, P Kα, Ca Kα, Y Lα, Th $M\alpha_1$, U $M\beta_1$, and Pb $M\beta_1$. Y Lα and P Kα are analysed on a PET crystal to obtain larger resolution than is possible on TAP; this avoids the P Kα–Y Lβ interference inherent in xenotime. Analysis of Pb Mβ (on a Xe detector) avoids the interference from second-order Ce Lα on Pb Mβ inherent in 140 mm Rowland circles coupled with Ar detectors, and the coupled Th Mz1,2 plus Y Lγ2,3 interference on Pb Mα. Interference of Th Mγ on U Mβ is corrected by application of an empirical correction factor combining measurement of Th Mα intensity plus apparent U Mβ intensity in the U-free Th standard and the Th Mα intensity in the unknown (Pyle *et al.*, 2005).

For the REE, the high concentrations of La, Ce and Nd in monazite generate problematic interferences between the Lβ and Lγ lines of the above elements and the Lα lines of the MREE (Nd–Tb). To avoid the need for interference corrections, intensities of the Lβ lines of Pr, Nd, Sm, Gd and Tb are measured in monazite. The Lβ line of Gd has a near-total overlap with Ho Lα, but

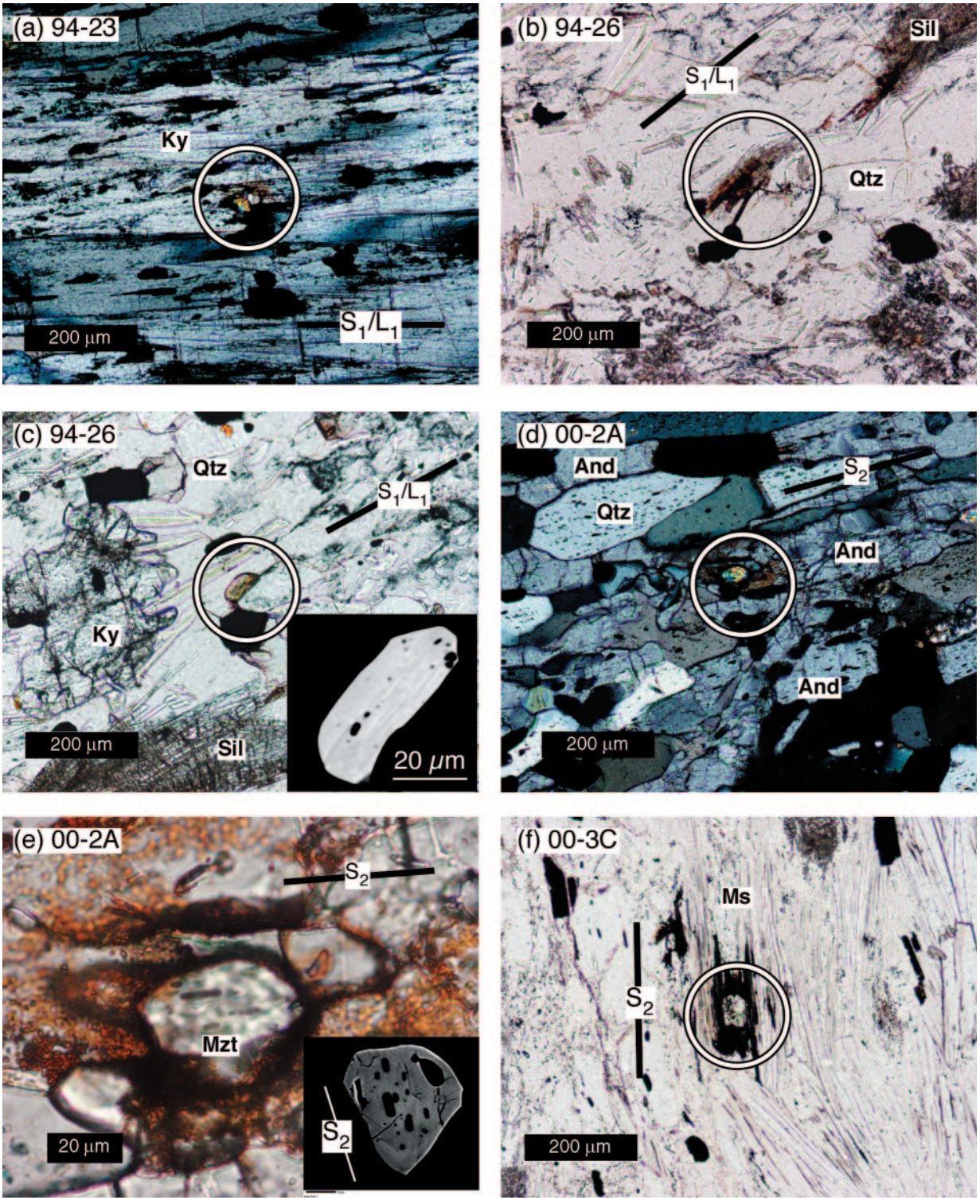

Fig. 5. Digital photomicrographs showing monazite textural relationships in cross-polarized and plane-polarized light. (a) Kyanite crystal with monazite inclusion from quartzite sample; both kyanite and monazite are aligned parallel to S_1 and L_1. (b) Quartzite sample with sillimanite overgrowing monazite, both aligned parallel to L_1. (c) Quartzite sample with matrix monazite grain aligned parallel to S_1 and L_1. Inset BSE image shows another monazite with titanhematite inclusions aligned in S_1 and L_1. (d) Andalusite porphyroblast with monazite inclusion from schist sample. (e) Detail of previous monazite (d) showing inclusion of titanhematite aligned parallel to S_2. Inset shows BSE image of aligned titanhematite inclusions in matrix monazite grain from sample 3c. (f) Schist sample showing monazite grain within matrix muscovite, both aligned parallel to S_2.

extremely low (generally $\leq$0·1 wt %) concentrations of Ho in monazite obviate the need for a Gd Lβ–Ho Lα interference correction.

Conversely, in xenotime, the generally low concentrations of LREE (La–Sm) result in negligible interference between Lβ and Lγ lines of the LREE and the Lα lines of the MREE. Therefore, the La lines of the MREE (Nd, Sm, Eu, Gd, Tb) in xenotime are measured. Ho Lβ is measured in xenotime so as to avoid Gd Lβ–Ho Lα interference. A final interference to be addressed is that of Tb Lβ on Er Lα. Er is a major component in xenotime, and usually below detection limits in monazite, whereas Tb is a minor component (0–1 wt %) in both REE phosphates, but slightly more abundant in xenotime (Scherrer *et al.*, 2000). It is preferable to correct Er Lα for Tb Lβ interference rather than analyse Er Lβ, because of the lower intensity of Er Lβ and the partial overlap of Er Lβ by Th $L\beta_2$. Tb Lα is analysed in xenotime to avoid Er Lα interference. Tb Lβ is chosen for monazite analysis despite its lower intensity, as Tb Lα in monazite is subject to partial overlap by the tail of Sm $L\beta_3$, and is close also to the Sm $L\beta_1$ peak.

Results

Back-scatter electron imaging and X-ray compositional maps of monazite from all samples reveal up to three distinct compositional domains that we interpret as core, intermediate and rim (Fig. 6). In the quartzite samples (Fig. 6a–d), the core domains are defined by high Th, with the intermediate domains having low U and Y, and the rim domains defined by moderate to high U, and Y. The irregular and embayed nature for many of the grains and truncated internal zoning suggests at least two periods of dissolution interspersed between the growth events (Fig. 6a and b). Several mapped grains did not display such a core, and probably reflect a cut through the edge of the grain. Yttrium zoning is relatively flat across the core and intermediate domains, and increases slightly along the rims. A few subhedral monazite inclusions in kyanite show only localized development of a high-U rim, suggesting the grain was well armoured from subsequent dissolution and reprecipitation events (Fig. 6c). Anhedral monazite inclusions in fractured kyanite (Fig. 6d) commonly show well-developed high-U rims. We suggest that such grains were not isolated from the matrix and experienced the same dissolution and growth events that are recorded by the matrix monazite. Monazite grains from the schist samples (00–2A and 00–3C) possess U and Th compositions and zonation patterns distinctly different from those seen in the quartzite samples. Chemical zoning is characterized by a high-U core, a low-U outboard zone and an intermediate-U rim (Fig. 6e). Elevated Th content generally corresponds to high U. Relatively high yttrium corresponds to the increasing uranium in the rim domains.

Multiple analyses were taken from selected monazite grains to document the compositional variation in monazite and xenotime grains from both the quartzite and schist samples (Fig. 7). Representative monazite and xenotime analyses are given in Tables 3 and 4, respectively. (A complete listing of the 87 monazite analyses used in this study is available online from the *Journal of Petrology* website at http://www.petrology.oupjournals.org.) Xenotime analyses (Fig. 7a) vary between X_{YPO_4} = 0·70–0·80 and X_{HREEPO_4} = 0·20–0·30. A rescaled view (Fig. 7b) of monazite analyses from Fig. 7a more clearly shows the compositional differences across the different domains. Core compositions are the most enriched in HREE and the intermediate domain is the most depleted in HREE. Significant enrichment in huttonite + brabantite components (up to 15–25%) characterize the core domains in both quartzite and schist samples (Fig. 7c).

Analyses (Table 3) indicate that actinide enrichment in the quartzite samples is due primarily to Th substitution (up to 21·9 wt % ThO_2). Thorium enrichment is not as extreme in the aluminous schist samples (up to 10·5 wt %), but monazite grains are highly enriched in U (up to 3·9 wt % UO_2), relative to monazite from the quartzite. The incorporation of actinides (Th, U) is accomplished by the brabantite, $Ca(Th,U)REE_{-2}$ and huttonite $(Th,U)SiREE_{-1}P_{-1}$ substitutions (Förster, 1998). Ce_2O_3 concentrations fall to as little as ~13 wt % in Th-rich monazite, with concomitant depletion in La_2O_3 (minimum 2·3 wt %).

Xenotime analyses from both quartzite and aluminous schist samples (Table 4) show some compositional variability, though back-scatter electron images show no detectable contrast variations within grains. X_{YPO_4} varies between 0·71 and 0·78. Major HREE components (Dy, Er, Yb) vary by no more than 2 wt % in analysed grains. X_{GdPO_4} ranges from 1·88 to 5·98 wt % and the higher concentrations correlate with lower X_{YPO_4}, consistent with xenotime growth during changing temperature conditions (Gratz & Heinrich, 1998).

Relative timing of monazite growth

Petrographic observations from the quartzite samples (Fig. 5a–c) and compositional zoning patterns observed in both matrix monazite and monazite included within kyanite (Fig. 6a–c) suggest that the monazite cores formed prior to the formation of kyanite. Intermediate and rim domains are interpreted to have grown in the kyanite stability field with rim domain growth probably extending into the sillimanite stability field for the schist samples. The alignment of titanhematite inclusions within aligned monazite (Fig. 5c) and aligned monazite included within aligned kyanite (Fig. 5a) strongly supports a history of progressive deformation during the formation of S_1 and L_1 in the quartzite samples.

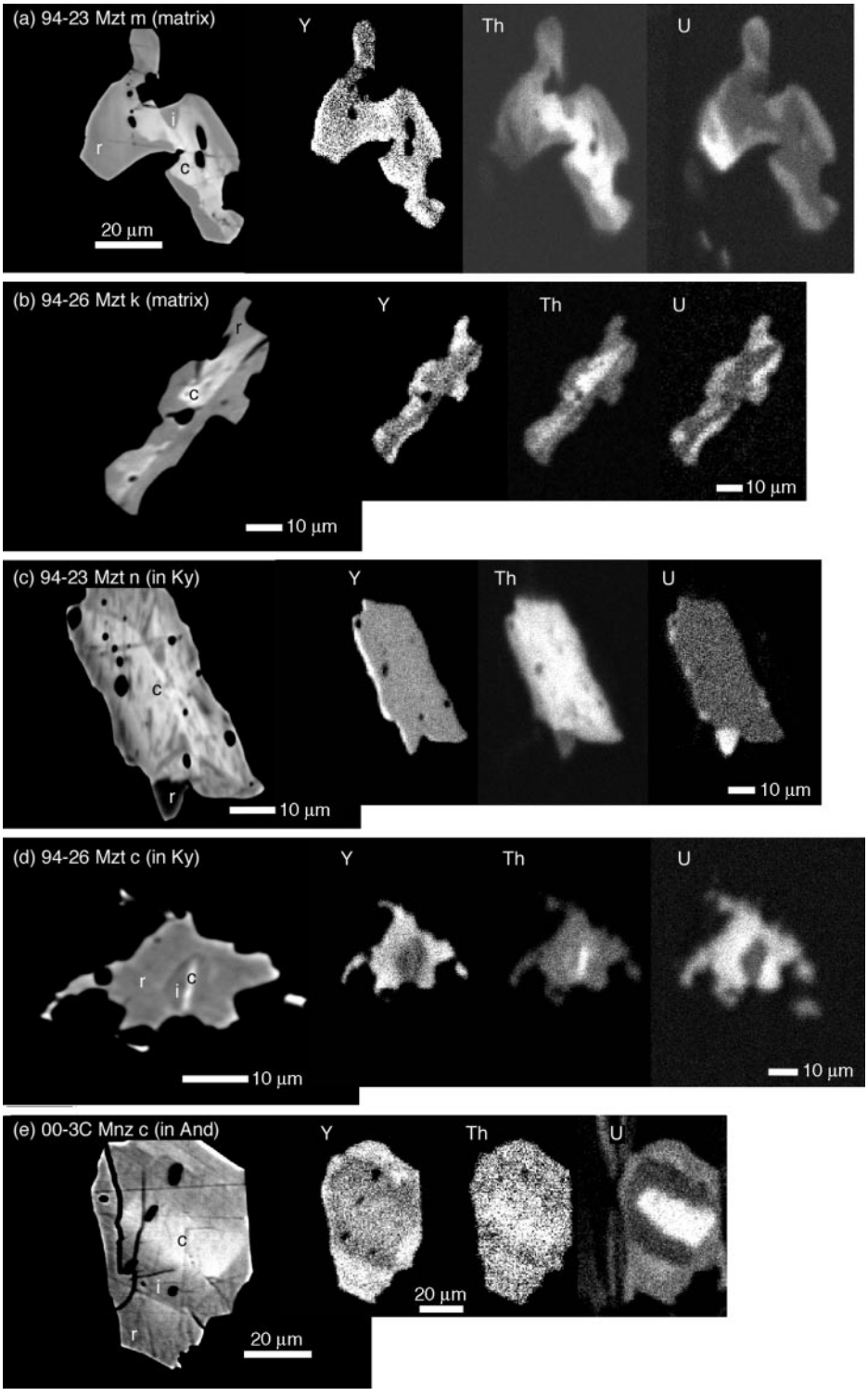

Fig. 6. Back-scatter electron images and compositional X-ray maps of selected monazite crystals, showing two or three distinct compositional domains (c, core; i, intermediate; r, rim). (a) and (b) Matrix monazite from quartzite showing irregular grain boundaries and truncated zoning interpreted as evidence of dissolution. (c) Monazite inclusion in kyanite from same sample as (a), showing subhedral to euhedral shape and very little development of an intermediate or rim domain. (d) Monazite inclusion in fractured kyanite showing anhedral grain shape and high-U rim similar to matrix monazite. (e) Representative monazite from the schist samples with three distinct compositional domains largely defined by variations in uranium. Similar zoning patterns were observed in both matrix monazite and monazite inclusions within andalusite and are interpreted to reflect growth of monazite prior to andalusite.

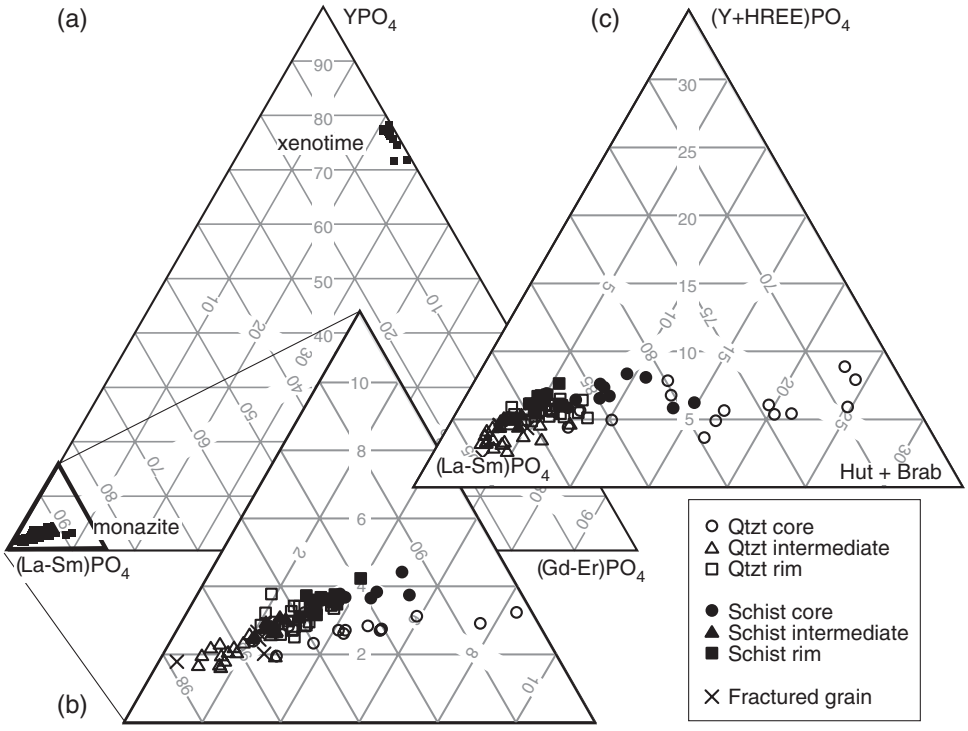

Fig. 7. (a) YPO_4–(La–Sm)PO_4–(Gd–Er)PO_4 diagram showing all monazite and xenotime analyses from all five samples. (b) Detailed view of monazite compositions from (a), showing core, intermediate and rim domains. (c) (Y+La–Sm)PO_4–(Huttonite+Brabantite)–LREEPO_4 diagram showing enrichment of huttonite and brabantite components in monazite core domains.

Monazite–xenotime geothermometry

Recent experimental and empirical studies have produced several calibrations of a monazite–xenotime solvus geothermometer (Gratz & Heinrich, 1997, 1998; Heinrich *et al.*, 1997; Pyle *et al.*, 2001; Seydoux-Guillaume *et al.*, 2002). The ability to determine both temperature and time from the same monazite provides a relatively well-constrained point on the *T–t* history of a metamorphic rock (Viskupic & Hodges, 2001). Furthermore, the monazite geothermometer can potentially be applied to metamorphic rocks that lack appropriate minerals for Fe–Mg exchange thermometry. The high closure temperature for REE diffusion in monazite (Cherniak *et al.*, 2004) potentially allows for the recovery of pre-peak metamorphic temperatures. We note that monazite is susceptible to partial (or complete) dissolution and regrowth, and examples of pelitic schist with multiple generations of monazite are well documented (Pyle & Spear, 2003).

Monazite–xenotime equilibrium

Application of the thermometers requires the equilibrium coexistence of monazite with xenotime. Xenotime is present in all samples, though only rarely in contact with monazite; monazite inclusions were also observed within xenotime in one sample. Experimental results in the system YPO_4–$GdPO_4$–$CePO_4$ show systematic partitioning of Y and Gd between coexisting monazite and xenotime such that, in monazite, both Y and Gd increase with increasing temperature, whereas in xenotime, Gd decreases and Y increases with increasing temperature (Gratz & Heinrich, 1998).

Given the chemical variations shown in the monazite grains from the Picuris, the potential for disequilibrium was carefully considered. A plot of X_{YPO_4} vs X_{GdPO_4} (Fig. 8a) shows monazite and xenotime compositions for all five samples. The high Gd, low Y xenotime are interpreted as early, relatively lower-temperature compositions; xenotime with low Gd and high Y are interpreted as later, relatively higher-temperature compositions. The presence of monazite with core Gd concentrations higher than most of the coexisting xenotime suggests monazite core growth in the absence of xenotime.

Figure 8b and c shows a rescaled view of the monazite compositions from Fig. 8a. Core Gd compositions in monazite from quartzite vary significantly from $X_{GdPO_4} = 0{\cdot}049$ to near $0{\cdot}015$, at near-constant $X_{YPO_4} = 0{\cdot}02$–$0{\cdot}025$. Monazites from schist samples show a similar trend, with $X_{GdPO_4} = 0{\cdot}02$–$0{\cdot}04$ at near-constant $X_{YPO_4} = 0{\cdot}03$–$0{\cdot}035$ for the schist samples (Fig. 8b). When core domains and three points interpreted as

Table 3: Selected monazite electron microprobe analyses and monazite–xenotime temperature estimates

Sample no.:	94–23	94–23	94–23	94–23	9426C	9426C	9426C	94–27	94–27	94–27	94–27	94–27	94–27	94–27	002A	002A	002A	002A	00–3C	00–3C	00–3C	00–3C	00–3C
Analysis no.:	21	22	23	26	101	102	103	10	11	12	23	38	39	40	115	116	124	125	5	6	7	6	7
Domain:	rim	core	inter.	core	core	inter.	rim	core	inter.	rim	rim	rim	rim	fracture	core	rim	core	rim	core	inter.	rim	core	inter.
Grain:	f	m	m	n	c	c	c	d	d	d	g	g	g	h	b	b	i	i	a	a	a	f	f
Grain setting:[1]	m	m	m	Ky	m	m	m	m	m	m	Ky	Ky	Ky	m	And	And	m	m	m	m	m	And	And
P_2O_5	29·83	28·14	29·75	27·84	28·23	30·36	30·11	28·90	29·58	29·82	29·35	29·26	28·90	31·75	30·31	30·33	30·16	30·56	29·81	29·72	29·38	29·59	28·84
SiO_2	0·12	1·05	0·18	1·57	1·03	0·12	0·09	0·62	0·13	0·12	0·04	0·09	0·10	0·25	0·11	0·05	0·07	0·15	0·03	n.d.	0·02	0·05	0·03
CaO	1·29	3·14	1·48	3·29	2·48	0·76	1·15	2·00	0·59	0·85	0·83	0·64	0·65	0·90	1·56	1·12	1·57	1·00	1·47	0·66	0·99	1·78	0·87
PbO	0·78	1·21	0·73	1·38	0·87	0·38	0·76	0·77	0·20	0·50	0·66	0·41	0·37	0·39	0·98	0·65	0·94	0·45	0·98	0·29	0·57	1·16	0·44
ThO_2	3·41	18·60	5·53	21·50	15·65	3·31	5·99	11·64	3·22	4·10	1·63	2·72	2·64	4·36	4·73	3·86	4·54	3·01	4·04	2·78	3·34	4·82	3·36
UO_2	2·71	0·23	1·62	0·19	n.d.	0·24	1·24	0·29	0·28	1·25	3·31	1·23	1·28	0·87	2·41	1·17	3·52	1·24	3·62	0·63	1·78	3·92	1·05
Y_2O_3	1·36	0·86	1·03	0·83	0·85	0·88	1·53	1·21	1·00	1·38	1·56	1·32	1·31	0·88	1·53	1·80	1·45	1·35	1·32	1·23	1·58	1·48	1·35
La_2O_3	13·57	4·99	10·25	3·84	5·24	15·32	12·55	4·78	12·08	14·87	13·68	13·73	13·68	17·17	7·76	12·36	6·96	13·68	11·57	15·73	14·33	9·22	15·06
Ce_2O_3	29·74	19·75	29·21	17·66	27·06	36·49	29·24	15·97	29·81	26·51	28·14	28·91	28·95	27·67	25·32	27·97	26·17	29·40	25·82	29·33	26·88	25·20	28·64
Pr_2O_3	2·61	2·83	3·14	2·73	3·02	2·63	2·74	3·37	3·85	3·16	3·10	3·23	3·35	3·06	3·40	3·02	3·25	2·92	3·20	3·26	3·13	3·30	3·06
Nd_2O_3	9·42	12·96	11·90	13·53	11·85	8·27	9·09	20·40	13·91	12·10	12·06	12·32	12·70	11·32	13·66	11·32	13·79	11·15	12·86	12·14	11·75	13·88	11·63
Sm_2O_3	1·42	2·30	1·62	2·78	2·28	1·35	1·71	7·24	1·94	2·21	2·19	2·23	2·30	1·87	2·95	2·11	2·89	2·12	2·16	1·92	2·04	2·61	1·97
Gd_2O_3	1·09	1·41	1·06	1·76	1·07	0·69	1·05	3·31	0·84	1·24	1·70	1·42	1·40	1·20	2·30	1·91	2·26	1·78	1·56	1·31	1·61	1·95	1·48
Tb_2O_3	0·10	0·10	0·12	0·11	n.d.	n.d.	n.d.	0·23	n.d.	n.d.	0·18	0·20	0·16	0·17	0·17	0·19	0·18	0·12	n.d.	0·16	0·20	0·16	0·15
Dy_2O_3	0·46	0·59	0·38	0·63	n.d.	n.d.	n.d.	n.d.	n.d.	n.d.	0·44	0·14	n.d.	0·37	0·28	0·46	0·28	n.d.	0·23	0·07	0·27	0·22	n.d.
Er_2O_3	0·08	0·07	0·06	n.d.	0·11	0·06	0·14	0·08	0·09	0·10	0·14	0·11	0·10	0·09	0·12	0·10	0·10	0·11	0·13	0·08	0·09	0·10	0·10
Total	97·99	98·22	98·06	99·68	99·85	100·92	97·46	100·82	97·55	98·29	99·00	97·96	97·90	102·33	97·57	98·42	98·13	99·04	98·91	99·33	97·97	99·43	98·01
Mole fraction																							
YPO_4	0·031	0·022	0·023	0·021	0·020	0·019	0·035	0·028	0·022	0·031	0·034	0·029	0·029	0·019	0·036	0·040	0·034	0·030	0·030	0·027	0·035	0·034	0·029
$(La–Sm)PO_4$	0·879	0·732	0·877	0·694	0·797	0·935	0·878	0·799	0·932	0·901	0·887	0·909	0·912	0·906	0·843	0·869	0·842	0·895	0·866	0·920	0·885	0·842	0·904
$(Gd–Er)PO_4$	0·024	0·033	0·023	0·039	0·017	0·010	0·017	0·051	0·013	0·019	0·033	0·026	0·022	0·024	0·041	0·037	0·041	0·028	0·027	0·022	0·030	0·034	0·023
$(Y+HREE)PO_4$	0·055	0·055	0·046	0·060	0·037	0·029	0·053	0·079	0·035	0·050	0·067	0·055	0·051	0·044	0·077	0·077	0·074	0·057	0·057	0·048	0·065	0·068	0·053
Brabantite[2]	0·061	0·163	0·069	0·172	0·120	0·032	0·065	0·095	0·028	0·045	0·044	0·033	0·032	0·041	0·075	0·052	0·080	0·041	0·076	0·032	0·049	0·088	0·041
Huttonite[2]	0·005	0·049	0·008	0·074	0·046	0·005	0·004	0·027	0·005	0·005	0·002	0·004	0·004	0·010	0·005	0·002	0·003	0·006	0·001	0·000	0·001	0·002	0·001
Monazite–xenotime temperature estimates (°C)[3]																							
G&H[4]	477		414			395	477		402	488	529	501	498	479		538		521		465	510		480
P	448		396			252	434		311	417	509	445	426	378		549		460		409	498		436
S-G	472		402			204	453		285	430	556	469	443	376		611		489		419	542		456

[1]m, matrix grain; Ky, And: inclusion in kyanite or andalusite.
[2]Brabantite: $Ca_{0.5}(Th,U,Pb)_{0.5}PO_4$; Huttonite: $(Th,U,Pb)SiO_4$.
[3]G&H (Gratz & Heinrich, 1998); P (Pyle *et al.*, 2001); S-G (Seydoux-Guillaume *et al.*, 2002).
[4]$X_{Gd} = Gd/\sum REE$.
n.d., element concentration below detection limit.

Table 4: Xenotime electron microprobe analyses

Sample:	94–23	94–26	94–26	94–26	00–2A	00–2A	00–2A	00–2A	00–3C	00–3C	00–3C	00–3C
Quant. no.:	1005	104	106	107	108	109	110	111	1	2	3	4
P_2O_5	34·02	35·09	35·28	35·11	36·40	35·91	35·90	35·61	35·31	34·53	35·47	35·23
SiO_2	0·19	0·27	0·90	0·44	n.d.	0·05	0·02	n.d.	n.d.	2·23	n.d.	n.d.
CaO	0·09	0·03	n.d.	0·07	0·07	0·02	0·04	0·04	0·09	0·05	0·09	0·09
PbO	n.d.	0·17	0·18	0·18	n.d.	n.d.	n.d.	0·23	n.d.	0·15	n.d.	n.d.
ThO_2	0·85	0·65	0·51	0·30	n.d.	n.d.	n.d.	n.d.	n.d.	n.d.	n.d.	n.d.
UO_2	0·12	n.d.	0·40	0·45	0·44	n.d.	0·14	0·25	0·33	0·59	0·44	0·38
Y_2O_3	39·53	41·57	41·14	37·21	41·09	40·83	41·80	41·30	41·20	40·33	41·43	40·78
Nd_2O_3	0·14	0·68	0·07	n.d.	0·28	0·18	0·24	0·27	0·24	0·31	0·26	0·24
Sm_2O_3	1·36	0·72	0·13	0·32	0·46	0·42	0·43	0·43	0·41	0·52	0·46	0·43
Eu_2O_3	0·99	0·12	n.d.	0·31	0·26	0·23	0·26	0·27	0·24	0·12	0·25	0·25
Gd_2O_3	5·98	2·44	1·88	3·59	2·54	2·32	2·46	2·39	2·42	2·37	2·52	2·49
Tb_2O_3	0·98	0·57	0·76	0·83	0·69	0·53	0·68	0·60	0·65	0·64	0·70	0·67
Dy_2O_3	6·26	5·12	5·62	7·47	5·97	5·49	5·88	5·94	6·03	5·69	5·98	5·90
Ho_2O_3	1·19	1·31	1·40	1·30	1·34	1·25	1·31	1·36	1·32	1·31	1·32	1·31
Er_2O_3	3·82	4·46	4·40	4·74	4·33	4·58	4·36	4·44	4·37	4·23	4·32	4·33
Tm_2O_3	0·61	0·63	0·48	0·66	0·61	0·70	0·49	0·41	0·62	0·61	0·54	0·46
Yb_2O_3	4·56	4·39	4·34	5·12	4·89	6·30	4·91	5·03	4·72	4·35	4·89	4·87
Total	100·79	98·23	97·55	98·14	99·45	98·85	98·92	98·64	98·09	98·10	98·77	97·51
YPO_4	0·708	0·766	0·776	0·711	0·757	0·756	0·767	0·761	0·761	0·763	0·759	0·759
$LREEPO_4$	0·029	0·018	0·003	0·008	0·012	0·010	0·011	0·012	0·011	0·012	0·012	0·011
$HREEPO_4$	0·252	0·208	0·212	0·271	0·224	0·233	0·220	0·221	0·221	0·217	0·221	0·222

mixed domain analyses are removed, the intermediate and rim domains show a systematic increase in Gd with increasing Y, suggesting growth in the presence of xenotime (Fig. 8c). Based on these observations only the intermediate and rim temperature estimates are interpreted as geologically significant.

Monazite–xenotime geothermometers

Monazite–xenotime temperature estimates from three calibrations are included in Table 3 for each intermediate and rim spot analysis, and are summarized in Table 5. The thermometer of Gratz & Heinrich (1998) is based upon the partitioning of Gd ($X_{Gd} = Gd/\sum REE$) between monazite and xenotime, and was experimentally calibrated for the system YPO_4–$CePO_4$–$GdPO_4$. Intermediate domain temperatures were calculated by pairing monazite compositions with the highest-Gd (low-temperature) xenotime analysed in the quartzite ($X_{Gd} = 0{\cdot}24$) and schist sample ($X_{Gd} = 0{\cdot}12$). Rim domain temperatures were calculated by pairing monazite compositions with the lowest-Gd (highest-temperature) xenotime analysed in the quartzite ($X_{Gd} = 0{\cdot}10$) and schist ($X_{Gd} = 0{\cdot}11$) samples. The accuracy of this calibration is given as approximately ±50°C.

The second calibration, by Pyle *et al.* (2001), is an empirical calibration (Y+HREE vs T) of the monazite limb of the monazite–xenotime solvus based upon selected monazite–xenotime pairs from New England. The third calibration, by Seydoux-Guillaume *et al.* (2002), is based upon experimental work in the $ThSiO_4$–$CePO_4$–YPO_4 system, and on earlier experimental results from Gratz & Heinrich (1997) in the binary system $CePO_4$–YPO_4. Results from Seydoux-Guillaume *et al.* (2002) suggest that YPO_4 in monazite increases with increasing $ThSiO_4$, producing a significant shift in the monazite limb of the solvus, and a narrowing of the monazite–xenotime miscibility gap. The calibration of Seydoux-Guillaume *et al.* (2002) has no constraints for temperatures below 700°C. The accuracy of these two solvus calibrations is estimated at approximately ±50°C. This uncertainty is a minimum value because of the poorly constrained lower-temperature portions of these calibrations, and the increasing steepness of the monazite limb of the solvus with decreasing temperature.

Comparison of intermediate and rim domain temperatures

The three calibrations show considerable variation between intermediate and rim domains and between

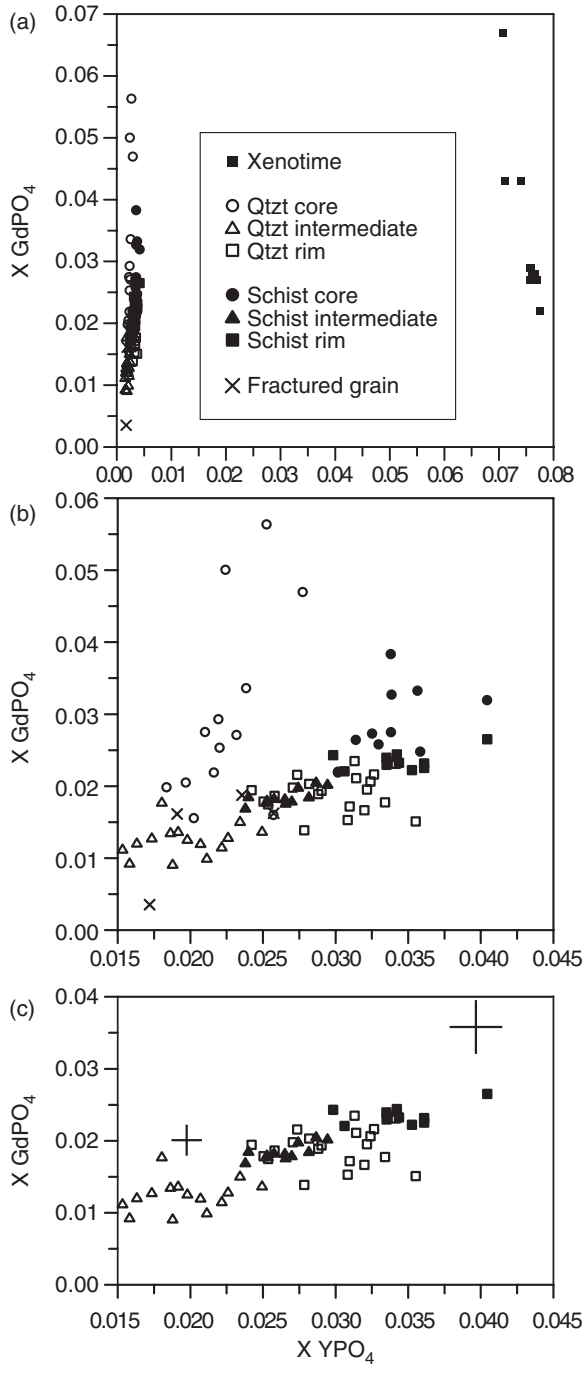

Fig. 8. (a) Plot of $GdPO_4$ versus YPO_4 for monazite and coexisting xenotime for all samples. Monazite core domains and matrix xenotime show variable Gd concentration. Monazite with Gd concentrations higher than coexisting xenotime suggests monazite growth in the absence of xenotime. (b) Close-up view of monazite analyses from (a), showing the compositional trends associated with the three domains. Core domains show variable Gd compositions at relatively constant YPO_4 in both quartzite and schist samples. (c) Same plot as (b) with core and mixed domain analyses removed to more clearly show compositional trends for the intermediate and rim domains. Analytical uncertainty for Gd and Y in monazite varies from 2 to 6%. Error bars of 5% are shown.

Table 5: Monazite–xenotime average domain temperatures (°C, 1 s.d.)

Sample and domain	G&H '98[1]	P[1]	S&G[1]
Schists (2A, 3C)			
Intermediate (12 pts)	470 (7)	415 (18)	427 (25)
Rim (10 pts)	517 (9)	498 (24)	542 (34)
Quartzites (23, 26, 27)			
Intermediate (15 pts)	405 (7)	316 (50)	291 (68)
Rim (21 pts)	501 (18)	455 (30)	482 (41)

[1]G&H '98 (Gratz & Heinrich, 1998); P (Pyle *et al.*, 2001); S-G (Seydoux-Guillaume *et al.*, 2002).

quartzite and schist samples (Table 5). Rim temperatures for the schist samples from all three calibrations are reasonable and fairly consistent with phase equilibria and petrographic observations. Rim temperatures from the quartzite samples are more variable with the calibration of Pyle *et al.* (2001), giving significantly lower temperature estimates. The quartzite samples also yield significantly lower intermediate domain temperatures, with very large standard deviations: ~315 ± 50°C and ~290 ± 68°C for the calibrations of Pyle *et al.* (2001) and Seydoux-Guillaume *et al.* (2002), respectively. These low temperatures are not consistent with monazite growth in the kyanite stability field, and probably reflect the lack of low-temperature data in the calibrations. These geologically unreasonable temperatures make comparison between domains and samples for the calibrations of Pyle *et al.* (2001) and Seydoux-Guillaume *et al.* (2002) unreasonable, and further discussion is limited to the results from the calibration of Gratz & Heinrich (1998).

The thermometer of Gratz & Heinrich (1998) yields intermediate domain temperatures of 405 ± 18°C for the quartzite samples and 470 ± 7°C for the schist samples. The difference in temperature is a result of the difference in the high-Gd (lowest-temperature) xenotime compositions measured in the quartzite ($X_{Gd} = 0{\cdot}24$) and schist ($X_{Gd} = 0{\cdot}12$) samples. This compositional difference and the corresponding temperature difference may be real. If this is the case, the temperature difference probably reflects a difference in bulk REE chemistry and reaction history. Alternatively, the temperature difference may reflect geological uncertainty in analysing and correlating the proper monazite and xenotime compositions. Xenotime grains are small (~5–15 μm long) and much less common than monazite in these samples; a total of eight xenotime grains were analysed in the two schist samples. It is possible that we did not locate and analyse the lowest-temperature, highest-Gd xenotime. If the schist sample did contain xenotime with a Gd concentration comparable with that of xenotime in the quartzite,

Table 6: Monazite ion microprobe isotopic analyses

Sample ID	Domain[1]	$^{207}Pb^*/^{235}U$ (1 s.e.)	$^{206}Pb^*/^{238}U$ (1 s.e.)	Corr. of concordia ellipses	$^{207}Pb^*/^{206}Pb^*$ (1 s.e.)	Age (Ma) $^{207}Pb^*/^{235}U$ (1 s.e.)	Age (Ma) $^{206}Pb^*/^{238}U$ (1 s.e.)	Age (Ma) $^{207}Pb^*/^{206}Pb^*$ (1 s.e.)	% Radiogenic ^{207}Pb (1 s.e.)	% Radiogenic ^{206}Pb (1 s.e.)
3c d_1	inter.	3·127 (0·1261)	0·2526 (0·01068)	0·961	0·08976 (0·00105)	1·439E+03 (31)	1·452E+03 (55)	1·420E+03 (22)	97.15 (0.083)	99.72 (0.008)
3c d_2	inter.	3·167 (0·0903)	0·2582 (0·00738)	0·994	0·08896 (0·00027)	1·449E+03 (22)	1·481E+03 (38)	1·403E+03 (6)	97.10 (0.092)	99.72 (0.009)
3c d_3	inter.	2·152 (0·0801)	0·1798 (0·00668)	0·986	0·08680 (0·00054)	1·166E+03 (26)	1·066E+03 (37)	1·356E+03 (12)	94.84 (0.197)	99.50 (0.019)
3c d_4	inter.	2·582 (0·1228)	0·2110 (0·01021)	0·974	0·08874 (0·00097)	1·296E+03 (35)	1·234E+03 (54)	1·399E+03 (21)	98.32 (0.057)	99.84 (0.005)
3c g_1	core	3·412 (0·0665)	0·2744 (0·00542)	0·973	0·09019 (0·00041)	1·507E+03 (15)	1·563E+03 (27)	1·430E+03 (9)	99.08 (0.019)	99.91 (0.002)
3c g_2	core	3·324 (0·0840)	0·2667 (0·00678)	0·971	0·09040 (0·00055)	1·487E+03 (20)	1·524E+03 (34)	1·434E+03 (12)	99.14 (0.018)	99.92 (0.002)
3c g_3	inter./rim	2·783 (0·0800)	0·2252 (0·00640)	0·981	0·08961 (0·00050)	1·351E+03 (21)	1·309E+03 (34)	1·417E+03 (11)	98.32 (0.037)	99.84 (0.004)
3c h_1	core/inter.	3·169 (0·0886)	0·2566 (0·00657)	0·931	0·08959 (0·00091)	1·450E+03 (22)	1·472E+03 (34)	1·417E+03 (20)	99.01 (0.023)	99.91 (0.002)
3c h_2	core/inter.	3·230 (0·0660)	0·2617 (0·00543)	0·990	0·08951 (0·00026)	1·464E+03 (16)	1·498E+03 (28)	1·415E+03 (6)	99.02 (0.023)	99.91 (0.002)
3c h_3	core	3·040 (0·0732)	0·2458 (0·00600)	0·990	0·08972 (0·00031)	1·418E+03 (18)	1·417E+03 (31)	1·420E+03 (7)	98.92 (0.025)	99.90 (0.002)
2a g_1	core	3·260 (0·1040)	0·2618 (0·00837)	0·978	0·09029 (0·00061)	1·471E+03 (25)	1·499E+03 (43)	1·432E+03 (13)	99.12 (0.020)	99.92 (0.002)
2a g_2	inter.	3·264 (0·1060)	0·2640 (0·00854)	0·998	0·08968 (0·00019)	1·472E+03 (25)	1·510E+03 (44)	1·419E+03 (4)	96.96 (0.087)	99.70 (0.009)
2a h_1	core/inter.	2·896 (0·1030)	0·2378 (0·00807)	0·958	0·08832 (0·00090)	1·381E+03 (27)	1·375E+03 (42)	1·390E+03 (20)	98.01 (0.044)	99.81 (0.004)
2a h_2	core	2·447 (0·0798)	0·1970 (0·00629)	0·987	0·09009 (0·00047)	1·257E+03 (24)	1·159E+03 (34)	1·427E+03 (10)	98.94 (0.027)	99.90 (0.003)
2a h_3	core/inter.	3·107 (0·1062)	0·2498 (0·00857)	0·989	0·09019 (0·00046)	1·434E+03 (26)	1·438E+03 (44)	1·430E+03 (10)	98.56 (0.049)	99.86 (0.005)

[1]Analysis overlapped domains as indicated.

then the average calculated temperature from 12 intermediate domains would be 422 ± 3°C, indistinguishable within precision from the quartzite sample.

Temperature estimates from the quartzite samples suggest that the intermediate monazite domain formed at temperatures near the kyanite-in isograd. Intermediate domain monazite growth in the schist samples may have occurred at similar temperatures or at somewhat higher temperatures of ~470°C. Regardless of this uncertainty, the schist samples yield results consistent with monazite growth at the lower to intermediate temperatures of the kyanite stability field, consistent with petrographic and chemical zoning observations.

Average temperatures for monazite rim domains are 501 ± 18°C and 517 ± 9°C, for the quartzite and schist samples, respectively. The maximum rim temperatures in the quartzite and the schist sample are 536 and 538°C, respectively. These temperatures are indistinguishable within analytical precision and consistent with peak temperature estimates previously determined in this study from phase equilibria. Monazite rim temperatures are also consistent with petrographic interpretations that suggest growth in the kyanite or possibly the sillimanite stability field.

Matrix monazite rims and monazite inclusions within fractured kyanite yield similar temperatures, suggesting partial dissolution and regrowth of monazite in kyanite. In the schist samples, monazite inclusions within andalusite and matrix monazite yield indistinguishable temperatures. The occurrence of monazite aligned in S_2, and included within andalusite that overgrows S_2, suggests that all monazite growth occurred prior to andalusite. The nearly continuous spread in monazite intermediate and rim compositions (Fig. 8c), and their corresponding temperatures, may reflect a process of dissolution and reprecipitation during progressive deformation and metamorphism rather than distinct monazite-forming events; minor disequilibrium at the thin-section scale may also be a factor. Three monazite rim analyses adjacent to fractures give temperatures of ~480 ± 8°C, and may reflect retrograde monazite growth.

Ion microprobe age determinations

Methods

Ion microprobe analyses of monazite were performed using the IMS 1270 ion microprobe at the Northeast National Ion Microprobe Facility at Woods Hole Oceanographic Institution. Raw data were reduced with ZIPS vs 2.4 and results imported into IsoPlot (Ludwig, 1999) for plotting and error analysis. Monazite standard UCLA76 (~336 Ma) was used for calibration of masses ^{232}Th, ^{248}ThO, ^{238}U, ^{254}UO–^{238}U, ^{204}Pb, ^{206}Pb, ^{207}Pb and ^{208}Pb. Reproducibility of the standard age based upon nine calibration points is 335 ± 7 Ma. Analytical time was ~60 s. No cycles were rejected for the unknowns.

Results

The ion microprobe analyses are summarized in Table 6; all ages are interpreted to represent the time of monazite growth. Two monazites from sample 00–2A and three monazites from sample 00–3C were analysed. Analysed monazite grains and compositional maps are shown in Fig. 9. U, Th and Pb concentrations from the analysed domains are presented in Table 7. All 15 analyses are shown on a U–Pb concordia (upper intercept age of 1417 ± 9 Ma) diagram (Fig. 10). The analysed monazite grains occur as inclusions within andalusite and matrix muscovite. Many of the ion probe analyses sampled across compositional domains and possibly age domains, and we are cautious in using these data to document the relative timing of core, intermediate and rim monazite growth. We note that the younger, discordant ages are typically from the second (or later) spot analysed on each grain, suggesting that sample charging may be responsible for the discordant analyses. ^{207}Pb–^{206}Pb age determinations from concordant and near-concordant analyses yield ages that range from 1434 ± 12 Ma (core) to 1390 ± 20 Ma (rim) and suggest monazite growth occurred over several million to a few tens of million years.

These ion microprobe ages are somewhat younger than the ~1450 Ma monazite ages reported by Williams *et al.* (1999), and the garnet (1461 ± 13 Ma) and staurolite (1454 ± 7 Ma) ages reported by Lanzirotti & Hanson (1997) for the southern Picuris. Electron microprobe chemical age determinations from more than 50 additional monazite grains from these samples, including monazite grain 'n' included within kyanite (Figs 6a and 7b), yield ages from ~1450 to ~1390 Ma (Pyle & Daniel, in preparation), and are consistent with the ion microprobe isotopic age determinations. We find no evidence of older, ~1650 Ma monazite in any of these five samples.

DISCUSSION

Discussion of monazite ages and a proposed *P–T–t–D* path

The absence of older (≥1650 Ma) monazite cores or inclusions requires that (1) we simply missed the older detrital or metamorphic cores or grains; or (2) these rocks experienced only a single, regional, amphibolite-facies metamorphic event beginning at 1450–1435 Ma; or (3) older detrital (>1700 Ma) or metamorphic (~1650 Ma) monazite grains dissolved completely prior to, or during, the ~1400 Ma metamorphism. Given the X-ray mapping and analysis of more than 50 monazite

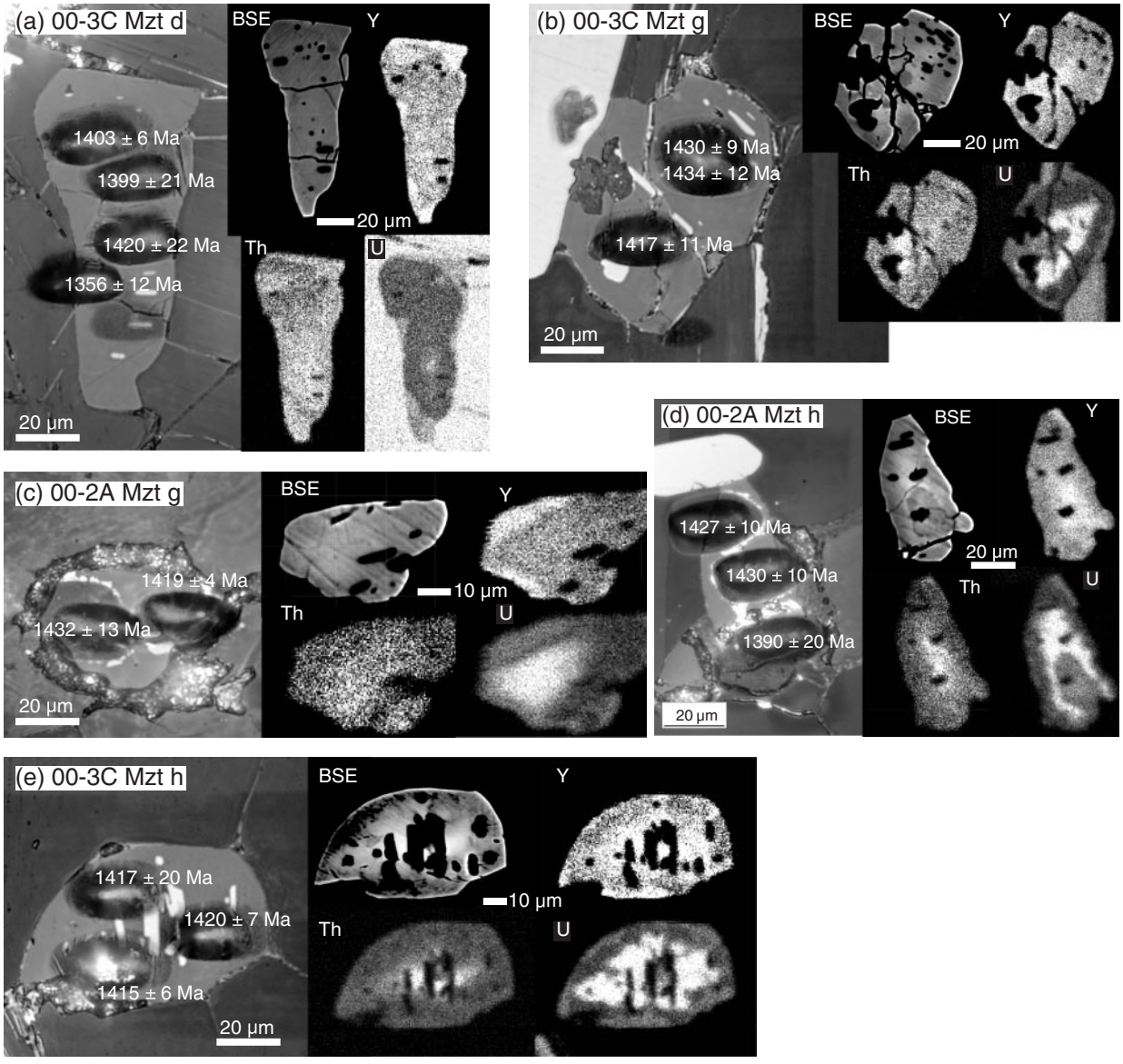

Fig. 9. Reflected light digital images, BSE images and X-ray compositional maps of Y, Th, U in monazite from the two schist samples. Dark pits represent the location of ion microprobe analyses and the associated ^{207}Pb–^{206}Pb isotopic age (±1 s.e.).

grains (includes EMP age analyses, from Pyle & Daniel, in preparation), from five samples and two different bulk compositions, we suggest that the first possibility seems remote.

Alternatively, these rocks experienced only a single *P–T* loop at 1450–1400 Ma, inconsistent with the models of polymetamorphism proposed by Karlstrom *et al.* (1997, 2004), Pedrick *et al.* (1998), Read *et al.* (1999) and Williams *et al.* (1999). In this case, the older monazite grains from the Tusas peaks may reflect contact metamorphism from ~1690 to ~1660 Ma plutons. The occurrence of aligned titanhematite within monazite indicates that S_1 was well established prior to ~1435 Ma. It is possible that this foliation reflects, in part, an older, ~1650 Ma deformation; however, the progressive nature of S_1 interpreted from the petrographic observations suggests otherwise. We interpret S_1, the regional, km-scale, F_2 folding and the S_2 transecting cleavage (Bauer, 1993) to have formed between ~1435 and ~1400 Ma. A summary *P–T–t–D* diagram (Fig. 11) places the monazite time and temperature data into context with respect to the Al_2SiO_5 polymorph reaction sequence and deformational fabrics.

Given recent work by Kopera (2002*a*, 2002*b*) that documents monazite with ~1400 Ma rims and either ~1650 or >1700 Ma cores from the adjacent Tusas range, we do

Table 7: U, Th, Pb concentrations[1] *of monazite domains from age determinations*

Sample ID	UO_2 wt %	% error	ThO_2 wt %	% error	PbO wt %	% error
3c mzt d_i	0·42	3·34	1·85	1·68	0·22	3·79
3c mzt d_r	1·04	1·59	1·94	1·61	0·31	2·75
3c mzt g_c	1·02	1·62	2·65	1·46	0·46	2·06
3c mzt g_r	0·89	1·75	2·60	1·46	0·34	2·43
3c mzt h_c	2·98	0·50	4·83	1·28	1·37	1·10
3c mzt h_i	0·64	2·50	2·54	1·50	0·31	2·70
2a mzt g c	2·13	1·09	2·63	1·48	0·69	1·73
2a mzt g_i	0·55	2·60	2·11	1·60	0·44	2·28
2a mzt h_c	2·70	0·63	3·88	0·82	0·60	1·03
2a mzt h_i	0·35	2·82	0·70	2·44	0·13	1·59
2a mzt h_r	1·13	0·96	2·73	0·88	0·29	1·49

[1]All analyses from electron microprobe.

not rule out the possibility that early ($\geq$1650 Ma) monazite was present in the Picuris range. If older monazite was present, then the very efficient dissolution of monazite, in the northern Picuris, presents an interesting problem regarding monazite stability and the processes of regional metamorphism and fluid flow. If the northern Picuris range did experience regional metamorphism near 1650 Ma, we suggest that peak metamorphic temperatures were probably much cooler ($\leq$400°C) than proposed by previous workers (Karlstom *et al.*, 1997, 2004; Williams *et al.*, 1999). We stand by our conclusion that the regional folding and thrusting occurred between 1450 and 1400 Ma.

Recent and continuing studies suggest that deformation related to the ~1400 Ma orogenic event is widespread. Proterozoic rocks in the Taos, Cimarron, Tusas, Rincon and Needle uplifts record the penetrative deformational effects of this event (Pedrick *et al.*, 1998; Read *et al.*, 1999; Williams *et al.*, 1999; Daniel & Pyle, 2001; Hallett *et al.*, 2002; Kopera *et al.*, 2002*a*, 2002*b*). Regional metamorphism and deformation also extends to the south at least as far as the Manzano uplift (Marcoline *et al.*, 1999; Ralser, 2000). Effects of this orogenic event also extend north into central Colorado (Selverstone *et al.*, 2000; Shaw *et al.*, 2001) and west into northern Arizona (Dumond *et al.*, 2004), where evidence is present for ~1400 Ma reactivation of older Proterozoic shear zones.

Crustal evolution of the Picuris from ~1690 to ~1630 Ma

Our favoured hypothesis is that these rocks experienced only a single major tectonothermal event between ~1450 and ~1400 Ma. Contrary to earlier tectonic interpretations (Bauer, 1993; Karlstrom *et al.*, 1997, 2004; Williams *et al.*, 1999), we propose that the Vadito–Hondo supracrustal sequence remained at relatively shallow crustal levels (2–8 km) between ~1690 and ~1630 Ma, and recorded no significant regional metamorphism or ductile deformation related to the Mazatzal Orogeny.

Field relations and proposed emplacement depths for the Cerro Alto metadacite, the Puntiagudo granite porphyry, the Rana quartz monzonite and the Penasco quartz monzonite exposed in the southern Picuris range support this hypothesis. Long (1974) and Bell (1985) reported a thin discontinuous, fine-grained border zone around the Puntiagudo pluton and a relatively uniform grain size approaching this zone. Long interpreted this zone as a chilled margin; however, Bell interpreted the border zone as an area of contact metamorphism. Both studies reported generally discordant intrusive contacts and locally near-concordant intrusive contacts. Long (1974) concluded that the emplacement depth for the Puntiagudo granite porphyry (~1685 Ma) was between 1 and 4 km, although Bell proposed a slightly deeper emplacement depth of 6–10 km. Both studies agreed that the Rana quartz monzonite (~1673 Ma) displays a chilled margin and sharply discordant contacts, and that emplacement depth was 3–6 km.

The Cerro Alto metadacite (~1630 Ma) shows a fine grain size and appears to be interlayered with amphibolites interpreted as basalt flows (Bell, 1985). Both Long (1974) and Bell (1985) estimated emplacement depths no greater than ~2 km, and both agreed this unit was probably a subvolcanic intrusion. However, Long (1974) and Bell (1985) disagreed about the timing of the metadacite. Long (1974) interpreted the Cerro Alto metadacite to be the oldest of the igneous bodies, coeval with the formation of the amphibolites in the Vadito Group. Bell (1985) interpreted the metadacite as the youngest based upon an inferred unconformity and a preliminary U–Pb zircon age of ~1630 Ma. Based upon the interpretations of Bell (1985), the three intrusions record an overall decrease in emplacement depth between approximately 1685 and 1630 Ma. There is little or no evidence of significant contact metamorphism from these plutons. Long (1974) and Bell (1985) estimated an emplacement depth of 8–13 km for the younger ~1435 Ma Penasco quartz monzonite, requiring burial between 1630 and 1435 Ma.

The Puntiagudo quartz monzonite (1685 Ma), Rana quartz monzonite (1673 Ma) and Cerro Alto metadacite (~1630 Ma) are all penetratively foliated, commonly display S–C fabrics and mylonitic zones, and are folded by F_2 (Bauer, 1993). The younger Penasco granite (~1436 Ma) shows much less deformation, characterized by the development of a moderate to weak foliation along the margin of the granite. Based upon these observations, regional deformation in the southern Picuris was

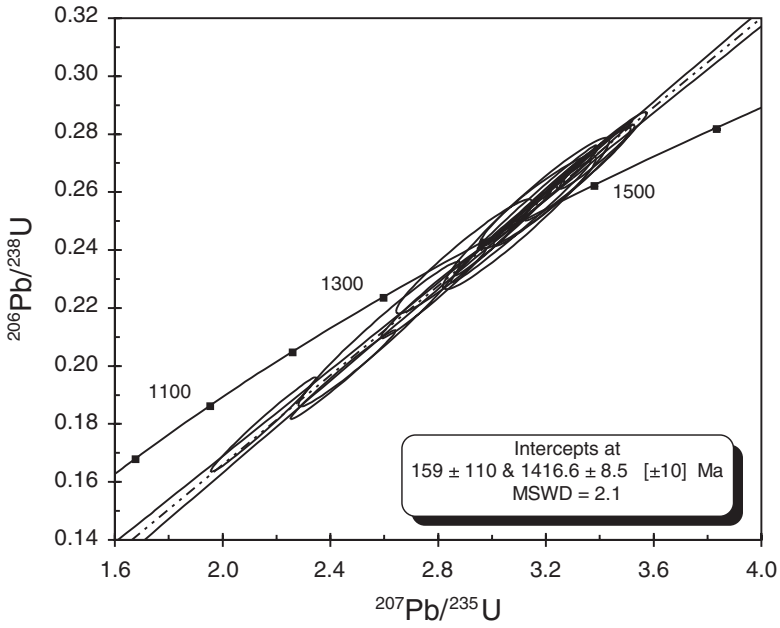

Fig. 10. (a) U–Pb concordia plot of 15 ion microprobe age determinations from the five analysed monazite grains.

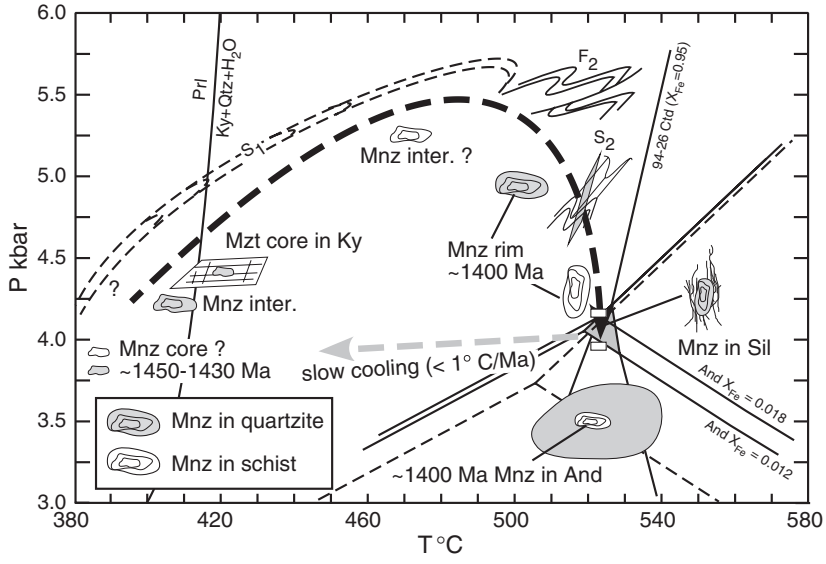

Fig. 11. Summary *P–T–t–D* diagram showing average monazite–xenotime temperature estimates for the intermediate and rim domains and the approximate age determinations for monazite core and rim domains. *P–T* conditions for monazite core domains are unknown. Peak metamorphic conditions (grey, triangular area) and relative timing of deformation events from Fig. 4. Slow cooling based upon regional ^{40}Ar–^{39}Ar cooling ages (Karlstrom *et al.*, 1997).

probably waning during the emplacement of the ~1435 Ma Penasco pluton or partitioned into different structural domains.

We do not dispute the regional evidence for the ~1650 Ma Mazatzal Orogeny across the southwestern USA (Karlstrom & Bowring, 1988, 1991; Bowring & Karlstrom, 1990; Bauer *et al.*, 1993; Bauer & Williams, 1994). We also agree that many areas in the southwestern USA record evidence of metamorphism and deformation related to tectonothermal events at both ~1650 and ~1400 Ma (Shaw *et al.*, 2001). However, we find no such evidence in the northern Picuris range. Clearly, considerable work is needed to understand the extent and tectonic significance of these events and to investigate the possible controls on monazite dissolution and growth.

ACKNOWLEDGEMENTS

We thank Chris Andronicos, Jane Gilotti and Frank Spear for discussions about various aspects of this work. Special thanks go to Graham Layne at WHOI for assistance in the acquisition of the ion microprobe analyses. We thank Matt Nyman for a day in the field many years ago. This work owes much to Dr Jeff Grambling (1953–1993), who introduced CGD to the Proterozoic geology of northern New Mexico. Constructive reviews from J. Hermann, Toti Larson and Mike Williams helped to significantly improve the manuscript and are much appreciated. We greatly appreciate the editorial handling of B. R. Frost. This work was supported by NSF award 0196116 to CGD. Funding for the Quanta 400 SEM and EDS system at Bucknell University was provided by the generous support of Bucknell University geology alumni, Bucknell University, and NSF award 0132204 to CGD.

SUPPLEMENTARY DATA

Supplementary data for this paper are available at *Journal of Petrology* online.

REFERENCES

Bauer, P. W. (1988). Precambrian geology of the Picuris Range, north-central New Mexico. *New Mexico Bureau of Mines and Mineral Resources Open-File Report* **OF-325**, 259 pp.

Bauer, P. W. (1993). Stratigraphic and structural evolution of Proterozoic rocks in the Picuris Range, Northern New Mexico. *Journal of Geology* **101**, 483–500.

Bauer, P. W. & Kelson, K. I. (1997). Preliminary geologic map of the Taos SW 7·5-minute quadrangle. *New Mexico Bureau of Geology and Mineral Resources Open File GM* **12**, scale 1:24 000.

Bauer, P. W. & Williams, M. L. (1989). Stratigraphic nomenclature of Proterozoic rocks, northern New Mexico: revisions, redefinitions and formalization. *New Mexico Geology* **11**, 45–52.

Bauer, P. W. & Williams, M. L. (1994). The age of Proterozoic orogenesis in New Mexico, USA. *Precambrian Research* **67**, 349–356.

Bauer, P. W., Karlstrom, K. E., Bowring, S. A., Smith, A. & Goodwin, L. (1993). Proterozoic plutonism and regional deformation: new constraints from the Manzano Mountains, central New Mexico. *New Mexico Geology* **15**, 49–55.

Bell, D. A. (1985). Structural and age relationships in the Embudo Granites, Picuris Mountains, New Mexico. M.S. thesis, University of Texas, Dallas, 175 pp.

Berman, R. G. (1988). Internally-consistent thermodynamic data for minerals in the system Na_2O–K_2O–CaO–MgO–FeO–Fe_2O_3–Al_2O_3–SiO_2–TiO_2–H_2O–CO_2. *Journal of Petrology* **29**, 445–522.

Bowring, S. A. & Karlstrom, K. E. (1990). Growth, stabilization and reactivation of Proterozoic lithosphere in the southwestern United States. *Geology* **18**, 1203–1206.

Carmichael, D. (1969). On the mechanism of prograde metamorphic reactions in quartz-bearing pelitic rocks. *Contributions to Mineralogy and Petrology* **20**, 244–267.

Cherniak, D. J., Watson, E. B., Grove, M. & Harrison, T. M. (2004). Pb diffusion in monazite: a combined RBS/SIMS study. *Geochimica et Cosmochimica Acta* **68**, 829–840.

Daniel, C. G. (1992). Metamorphic *P–T* paths from kyanite–sillimanite–andalusite-bearing rocks in north-central New Mexico. M.S. thesis, University of New Mexico, Albuquerque, 97 pp.

Daniel, C. G. & Pyle, J. (2001). Evidence for regional ~1·4 Ga metamorphism in the Rincon Range, north-central New Mexico: preliminary results from electron microprobe chemical age dating of monazite. *Geological Society of America, Abstracts with Programs* **33**, A-143.

Dumond, G., Williams, M., Mahan, K., Karlstrom, K. E. & Heizler, M. T. (2004). Tectonic heredity in the Grand Canyon and implications for Tibetan-scale Mesoproterozoic intra-continental deformation in the southwestern United States. *Geological Society of America, Abstracts with Programs* **36**, 403.

Förster, H.-J. (1998). The chemical composition of REE–Y–Th–U-rich accessory minerals in peraluminous granites of the Erzgebirge–Fichtelgebirge region, Germany, Part I: the monazite–(Ce)–brabantite solid solution series. *American Mineralogist* **83**, 259–272.

Grambling, J. A. (1981). Kyanite, sillimanite, andalusite, and related mineral assemblages in the Truchas Peaks region, New Mexico. *Contributions to Mineralogy and Petrology* **94**, 149–164.

Grambling, J. A. & Williams, M. L. (1985). The effects of Fe^{3+} and Mn^{3+} on aluminum silicate phase relations in north-central New Mexico, USA. *Journal of Petrology* **26**, 324–354.

Gratz, R. & Heinrich, W. (1997). Monazite–xenotime thermobarometry: experimental calibration of the miscibility gap in the binary system $CePO_4$–YPO_4. *American Mineralogist* **82**, 772–780.

Gratz, R. & Heinrich, W. (1998). Monazite–xenotime thermometry. III: Experimental calibration of the partitioning of Gd between monazite and xenotime. *European Journal of Mineralogy* **10**, 579–588.

Hallett, B. W., Daniel, C. G. & Pyle, J. (2002). ~1·4 Ga partial melting and regional deformation in Proterozoic migmatites of the Rincon range, north-central New Mexico: application of U–Th–Pb chemical dating. *Geological Society of America, Abstracts with Programs* **34**, A-67.

Heinrich, W., Andrehs, G. & Franz, G. (1997). Monazite–xenotime miscibility gap thermometry. I: An empirical calibration. *Journal of Metamorphic Geology* **15**, 3–17.

Holdaway, M. J. (1978). Significance of chloritoid-bearing and staurolite-bearing rocks in the Picuris Mountains, New Mexico. *Geological Society of America Bulletin* **89**, 1404–1414.

Holdaway, M. J. & Goodge, J. W. (1990). Rock pressure vs. fluid pressure as a controlling influence on mineral stability: an example from New Mexico. *American Mineralogist* **75**, 1043–1058.

Karlstrom, K. E. & Bowring, S. A. (1988). Early Proterozoic assembly of tectonostratigraphic terranes in southwestern North America. *Journal of Geology* **96**, 576–591.

Karlstrom, K. E. & Bowring, S. A. (1991). Styles and timing of Early Proterozoic deformation in Arizona: constraints on tectonic models. In: Karlstrom, K. E. (ed.) *Proterozoic Geology and Ore Deposits of Arizona. Arizona Geological Society Digest* **19**, 1–10.

Karlstrom, K. E., Dallmeyer, R. D. & Grambling, J. A. (1997). $^{40}Ar/^{39}Ar$ evidence for 1·4 Ga regional metamorphism in New Mexico: implications for thermal evolution of lithosphere in Southwestern USA. *Journal of Geology* **105**, 205–223.

Karlstrom, K. E., Amato, J. M., Williams, M. L., Heizler, M., Shaw, C., Read, A. & Bauer, P. (2004). Proterozoic tectonic evolution of the New Mexico region: a synthesis. In: Mack, G. H. & Giles, K. A. (eds) *The Geology of New Mexico. New Mexico Geological Society Special Publication* **11**, 1–34.

Kopera, J., Williams, M. L. & Jercinovic, M. J. (2002*a*). Monazite geochronology of Proterozoic quartzites: a powerful tool for understanding reactivation of continental lithosphere in the southwestern United States. *Geological Society of America, Abstracts with Programs* **34**(1), A-26.

Kopera, J., Williams, M. L. & Jercinovic, M. J. (2002*b*). Age constraints on fabric reactivation in the Tusas Range, northern New Mexico using electron microprobe monazite geochronology: Implications for the nature of regional ~1·4 Ga deformation. *Geological Society of America, Abstracts with Programs* **34**(6), 180.

Lanzirotti, A. & Hanson, G. N. (1997). An assessment of the utility of staurolite in U–Pb dating of metamorphism. *Contributions to Mineralogy and Petrology* **129**, 352–365.

Long, L. E. (1974). Contrasting types of Precambrian granitic rocks in the Dixon–Penasco area, northern New Mexico. *New Mexico Geological Society Guidebook* **25**, 101–108.

Ludwig, K. R. (1999). Isoplot/Ex version 2.10: a geochronological tool kit for Microsoft Excel. *Berkeley Geochronology Center Special Publication* **1**, 1–49.

Marcoline, J. R., Heizler, M. T., Goodwin, L. B., Ralser, S. & Clark, J. (1999). Thermal, structural, and petrological evidence for 1400-Ma metamorphism and deformation in central New Mexico. *Rocky Mountain Geology* **34**, 93–119.

Montgomery, A. (1953). Precambrian geology of the Picuris Mountains, north-central New Mexico. *New Mexico Bureau of Mines and Mineral Resources Bulletin* **30**, 89 pp.

Pattison, D. R. M. (1992). Stability of andalusite and sillimanite and the Al_2SiO_5 triple point: constraints from the Ballachulish aureole, Scotland. *Journal of Geology* **100**, 423–446.

Pedrick, J. N., Karlstrom, K. E. & Bowring, S. A. (1998) Reconciliation of conflicting tectonic models for Proterozoic rocks of northern New Mexico. *Journal of Metamorphic Geology* **16**, 687–707.

Pyle, J. M. & Spear, F. S. (2003). Four generations of accessory phase growth in low-pressure migmatites from SW New Hampshire. *American Mineralogist* **88**, 338–351.

Pyle, J. M., Spear, F. S., Rudnick, R. L. & McDonough, W. F. (2001) Monazite–xenotime–garnet equilibrium in metapelites and a new monazite–garnet thermometer. *Journal of Petrology* **42**, 2083–2107.

Pyle, J. M., Spear, F. S., Wark, D. A., Daniel, C. G. & Storm, L. C. (2005). Contributions to precision and accuracy of monazite microprobe ages. *American Mineralogist* **90**, 547–577.

Ralser, S. (2000). Microstructural constraints on the timing of Proterozoic deformation in Central New Mexico. *Journal of Metamorphic Geology* **18**, 457–466.

Rao, B. B. & Johannes, W. (1979). Further data on the stability of staurolite + quartz and related assemblages. *Neues Jahrbuch für Mineralogie, Monatshefte* **10**, 437–447.

Read, A. S., Karlstrom, K. E., Grambling, J. A., Bowring, S. A., Heizler, M. & Daniel, C. (1999). A middle-crustal cross section from the Rincon Range, northern New Mexico: evidence for 1·68-Ga, pluton-influenced tectonism and 1·4-Ga regional metamorphism. *Rocky Mountain Geology* **34**, 67–91.

Richardson, S. W. (1968). Staurolite stability in a part of the system Fe–Al–Si–O–H. *Journal of Petrology* **9**, 467–488.

Roeder, P. L. (1985). Electron-microprobe analysis of minerals for rare-earth elements: use of calculated peak-overlap corrections. *Canadian Mineralogist* **23**, 263–271.

Scherrer, N. C., Engi, M., Gnos, E., Jakob, V. & Leichti, A. (2000). Monazite analyses: from sample preparation to microprobe age dating and REE quantification. *Schweizerische Mineralogische und Petrographische Mitteilungen* **80**, 93–105.

Selverstone, J., Hodges, M., Aleinikoff, J. N. & Fanning, C. M. (2000). Mesoproterozoic reactivation of a transcurrent boundary in northern Colorado Front Range: implications for ~1·7- and 1·4-Ga tectonism. *Rocky Mountain Geology* **35**, 132–162.

Seydoux-Guillaume, A.-M., Wirth, R., Heinrich, W. & Montel, J.-M. (2002). Experimental determination of thorium partitioning between monazite and xenotime using analytical electron microscopy and X-ray diffraction Rietveld analysis. *European Journal of Mineralogy* **14**, 869–878.

Shaw, C. A., Karlstrom, K. E., Williams, M. L., Jercinovic, M. J. & McCoy, A. M. (2001). Electron microprobe monazite dating of ca. 1·71–1·63 Ga and ca. 1·45–1·38 Ga deformation in the Homestake shear zone, Colorado: origin and early evolution of a persistent intracontinental tectonic zone. *Geology* **29**, 739–742.

Viskupic, K. & Hodges, K. V. (2001). Monazite–xenotime thermochronometry: methodology and an example from the Nepalese Himalaya. *Contributions to Mineralogy and Petrology* **141**, 233–247.

Williams, M. L., Karlstrom, K. E., Lanzirotti, A., Read, A. S., Bishop, J. L., Lombardi, C. E., *et al.* (1999). New Mexico middle-crustal cross sections: 1·65-Ga macroscopic geometry, 1·4-Ga thermal structure, and continued problems in understanding crustal evolution. *Rocky Mountain Geology* **34**, 53–66.